Genetic dissection of crossover mutants defines discrete intermediates in mouse meiosis

Tolkappiyan Premkumar[1,2], Lakshmi Paniker[1], Rhea Kang[1,2,3], Mathilde Biot[1,4], Ericka Humphrey[1,5], Honorine Destain[1,6], Isabella Ferranti[1], Iyinyeoluwa Okulate[1], Holly Nguyen[1], Vindhya Kilaru[1], Melissa Frasca[1,2], Parijat Chakraborty[1], and Francesca Cole[1,2,*].

[1]Department of Epigenetics and Molecular Carcinogenesis, The University of Texas MD Anderson Cancer Center, Houston, Texas, USA

[2]The University of Texas MD Anderson Cancer Center UTHealth Houston Graduate School of Biomedical Sciences, Program in Genetics and Epigenetics, Houston, Texas, USA

[3]Present address: Luminex Inc., Austin, Texas, USA

[4]Present address: Institut de Génétique Humaine, University Montpellier, France; Centre National de la Recherche Scientifique, University Montpellier, France

[5]Present address: The University of Texas MD Anderson Cancer Center UTHealth Houston Graduate School of Biomedical Sciences, Program in Genetics and Epigenetics, Houston, Texas, USA

[6]Present address: Committee on Development, Regeneration, and Stem Cell Biology, University of Chicago, Chicago, IL, USA.

*Correspondence: FCole@MDAnderson.org @ColeFrancesca

Abstract

Crossovers, the exchange of homolog arms, are required for accurate segregation during meiosis. Studies in yeast have established that the single end invasion intermediate is highly regulated to ensure crossover distribution. Single end invasions are thought to differentiate into double Holliday junctions that are resolved by MutLgamma (MLH1/3) into crossovers. Currently, we lack knowledge of early steps of mammalian crossover recombination or how intermediates are differentiated in any organism. Using comprehensive analysis of recombination and cytology, we infer that polymerized single-end invasion intermediates and nicked double Holliday junctions are crossover precursors in mouse spermatocytes. In marked contrast to yeast, MLH3 plays a structural role to differentiate single end invasions into double Holliday junctions with differentially polymerized 3' ends. Therefore, we show independent genetic requirements for precursor formation and asymmetry with regard to 3' end processing, providing mechanistic insight into crossover formation and patterning.

20 **Introduction**

21 The fundamental mandate of meiosis is to generate haploid gametes from diploid precursors by
22 first segregating parental chromosomes (homologs) and then sister chromatids. Homolog segregation
23 is a challenge because chromosomes must be physically connected for accurate segregation, but only
24 identical sister chromatids are tethered by cohesion. The solution in most organisms, including humans
25 and mice, is to ensure homologous recombination as a crossover (CO) occurs between each homolog
26 pair (Gray and Cohen, 2016; Hunter, 2015) while maintaining sister chromatid cohesion to physically
27 tether homologs. Failure to ensure crossing over causes aneuploidy, and in humans, even mild CO
28 defects cause infertility, miscarriages, and constitutional aneuploidies such as Down syndrome
29 (Hassold and Hunt, 2001).

30 Meiotic recombination is initiated by SPO11-induced DNA double-strand breaks (DSBs) that
31 form preferentially at hotspots (Keeney et al., 2014). DSBs undergo resection that requires 5'→3'
32 exonucleolytic digestion by Exo1 in yeast, but not in mouse (Mimitou and Keeney, 2018; Yamada et al.,
33 2020; Zakharyevich et al., 2010). Resected 3´ overhangs form nucleoprotein filaments with DMC1 and
34 RAD51 that engage in strand invasion to form a nascent three stranded D-loop (Gray and Cohen,
35 2016) (**Figure 1A**). COs are designated in early meiotic prophase (Borner et al., 2004), a step that in
36 yeast requires Zip3 and MutSgamma, among other proteins and can be physically detected as a
37 metastable strand exchange intermediate, the single-end invasion (SEI) (Hunter and Kleckner, 2001).
38 These SEIs are thought to undergo second end capture to become double Holliday junctions (dHJs)
39 that are ultimately resolved as COs (Hunter, 2015). In mammals, the Zip3 ortholog RNF212 stabilizes
40 MutSgamma at recombination sites and is thought to be similarly required for CO designation (Qiao et
41 al., 2014; Rao et al., 2017; Reynolds et al., 2013). HEI10, an E3 ubiquitin ligase antagonizes RNF212's
42 role in MutSgamma stabilization, but is also required for CO maturation, the step in which dHJs are
43 resolved to form COs (Qiao et al., 2014; Ward et al., 2007). Proper CO maturation requires
44 MutLgamma, a heterodimer MLH1 and MLH3 (Gray and Cohen, 2016), which is thought to function as
45 a dHJ resolvase. Congruent with this model, MLH1 and MLH3 accumulate as foci at CO sites in

46 mammals and MutLgamma-derived COs require the nuclease function of MLH3 (Gray and Cohen,
47 2016; Nishant et al., 2008; Raghavan, 2019; Toledo et al., 2019). Indeed, reconstituted MutLgamma
48 complex containing a nuclease-dead allele of MLH3 lacks nicking activity in vitro (Cannavo et al., 2020;
49 Kulkarni et al., 2020). When MutLgamma is absent, only 1 – 2 COs are formed per mouse
50 spermatocyte and can be detected as connected homologs (bivalents) in metaphase (Guiraldelli et al.,
51 2013; Lipkin et al., 2002; Ward et al., 2007; Zelazowski et al., 2017). These COs are likely produced by
52 structure selective endonucleases (SSNs) such as MUS81 (Holloway et al., 2008).

53 Most DSBs in mammals (~90%) are repaired as noncrossovers (NCOs) - short patch-like repair
54 products that do not involve exchange of homolog arms (Cole et al., 2012b). Most NCOs form via
55 synthesis-dependent strand-annealing (SDSA) (Allers and Lichten, 2001) a process that does not
56 involve formation of a dHJ. In wildtype (WT) mouse and human spermatocytes, NCOs mostly
57 incorporate only one polymorphism from the donor, hence referred to as singletons (Cole et al., 2010;
58 Jeffreys and May, 2004). In mammals, only ~10% of DSBs are thought to be designated to form COs
59 during early meiotic prophase. In the absence of MLH3, these designated COs are acted upon by
60 alternative repair pathways to produce long NCOs called co-conversions that involve multiple
61 polymorphisms (Zelazowski et al., 2017).

62 In yeast, Exo1 plays an indispensable and nuclease-independent role in CO maturation by
63 MutLgamma (Gioia et al., 2021; Keelagher et al., 2011; Zakharyevich et al., 2010). Consonant with this
64 function, EXO1 can stimulate MutLgamma nicking activity in association with MutSgamma and RFC-
65 PCNA in vitro (Cannavo et al., 2020; Kulkarni et al., 2020). *Exo1*$^{-/-}$ mice are sterile and have ~80%
66 fewer COs, but only ~10% fewer MLH1/3 foci than WT spermatocytes (Kan et al., 2008; Wei et al.,
67 2003). Mice harboring the nuclease-dead allele of *Mlh3* (*Mlh3*^{DN}) also show disproportionately fewer
68 COs despite proficient MLH1/MLH3 focus formation (Toledo et al., 2019). The CO promoting role of
69 EXO1 is also nuclease-independent as mice carrying a nuclease dead allele of *Exo1* (*Exo1*^{D173A}) are
70 fertile and proficient in CO formation (Wang et al., 2022). Unlike yeast, the CO phenotype in mice

lacking EXO1 or MutLgamma are not similar raising the question of whether mammalian EXO1 and MLH3 play distinct roles in CO intermediate formation.

Much of our understanding of CO mechanisms is extrapolated from studies in yeast. This is in part due to detection of early CO precursor intermediates (Hunter and Kleckner, 2001; Schwacha and Kleckner, 1995) and retention of extensive heteroduplex when mismatch repair is compromised by deletion of Msh2 (Ahuja et al., 2021; Marsolier-Kergoat et al., 2018; Martini et al., 2011). However, CO precursors haven't been isolated in mammals and there are many unique features of recombination including infrequently retained heteroduplex (Peterson et al., 2020) As such, we lack understanding of the early steps of CO recombination. Using fine-scale, comprehensive analysis of recombination outcomes and cytology of 12 different mutant or mutant combinations, we provide evidence for two transient states of designated CO intermediates and define the roles of EXO1 and MLH3 in mouse spermatocytes. Key findings are that 1) the designated CO intermediate polymerizes from a single invaded 3' end likely forming an extended SEI intermediate; 2) MLH3 plays an unexpected structural role to differentiate the SEI intermediate into a dHJ; 3) CO precursor processing is asymmetric with regard to extent of 3' polymerization, which can explain CO biased resolution and patterning; and 4) the MLH3-structure dependent dHJs are more likely to be resolved as COs by SSNs.

87 **Results and Discussion**

88 **Mouse spermatocytes lacking EXO1 have disproportionately fewer COs than recombination**
89 **intermediates**

90 In budding yeast, loss of MutLgamma and Exo1 show similar phenotypes (Zakharyevich et al.,
91 2010) precluding epistatic analysis of null alleles. In mice, however, inactivation of *Exo1* does not share
92 a similar phenotype to *Mlh1*$^{-/-}$ or *Mlh3*$^{-/-}$ (Kan et al., 2008). We find that *Exo1*$^{-/-}$ spermatocytes have fewer
93 DMC1 foci in zygonema (155.8 ± 60) than WT or *Exo1*^{het} (224.0 ± 72.2 and 196.5 ± 60.45, respectively)
94 (**Figure 1B**). By contrast, loss of MLH3, shows equal numbers of recombination intermediates (RAD51
95 and gammaH2AX) in early zygonema as WT, although there are fewer RAD51 foci in late zygonema in
96 *Mlh3*$^{-/-}$ spermatocytes (Toledo et al., 2019). Similarly, there are lower RPA2 foci in *Mlh3*$^{-/-}$
97 spermatocytes in zygonema, but equivalent numbers in pachynema (Zelazowski et al., 2017). Lower
98 numbers of DMC1 foci could reflect reduced overall DSBs, reduced resection, or an overall reduction in
99 lifespan of the DMC1 nucleoprotein filament. Exo1 is required for most meiotic DSB resection in
100 budding yeast (Garcia et al., 2011; Keelagher et al., 2011; Mimitou and Keeney, 2018; Zakharyevich et
101 al., 2010), however loss of EXO1 nuclease activity lowers DSB resection by only 10% in the mouse
102 (Paiano et al., 2020; Yamada et al., 2020). While it is possible that *Exo1*$^{-/-}$ spermatocytes have fewer
103 DSBs, this is not found in budding yeast (Keelagher et al., 2011; Zakharyevich et al., 2010). Further,
104 axis lengths, which are usually proportional to meiotic DSB frequency (Keeney et al., 2014) are
105 unchanged between WT and *Exo1*$^{-/-}$ pachytene spermatocytes (**Figure S1A**). Finally, total
106 recombination frequency measured at the *59.5* hotspot in *Exo1*$^{-/-}$ diplotene spermatocytes (196.7 per
107 10,000 haploid genome equivalents) is similar to both WT (213.3), *Mlh3*$^{-/-}$ (194.6), and several other
108 mutants that do not show alteration in meiotic DSB frequency (**Table 1**, **Figure S1B**) (Rao et al., 2017;
109 Ward et al., 2007). We suggest reduced DMC1 foci in *Exo1*$^{-/-}$ spermatocytes reflects a combination of
110 mildly reduced resection and lifespan of the DMC1 nucleoprotein filament.

111 The 26% fewer DMC1 foci in *Exo1*$^{-/-}$ spermatocytes should be easily mitigated by CO
112 homeostasis (Martini et al., 2006), which in mouse spermatocytes ensures CO number despite mild

113 fluctuations in the overall number of early recombination intermediates (Cole et al., 2012a). However
114 similar to earlier reports in oocytes (Kan et al., 2008), we find only 20.0 ± 3.6 MLH1 foci per cell on
115 average in *Exo1*$^{-/-}$ spermatocytes as compared to 22.3 ± 2.5 and 22.4 ± 2.3 in WT and *Exo1*^{het},
116 respectively (**Figure 1C**). We find a similar ~10% reduction in MLH3 foci. The lower number of
117 MutLgamma foci could reflect a role(s) for EXO1 in CO homeostasis and in support of this model, *Exo1*$^{-}$
118 $^{/-}$ yeast have reduced CO interference (Gioia et al., 2021) – the observation that COs are further apart
119 than expected by chance. Reduced CO interference is seen when CO homeostasis is compromised
120 (Wang et al., 2015). However, we find that CO interference as measured by the coefficient of
121 coincidence of MLH1 foci is unchanged in *Exo1*$^{-/-}$ spermatocytes as compared to wild type (**Figure**
122 **S1C)**. Alternatively, EXO1 could play a role in the lifespan or stability of the MutLgamma complex, in
123 support of this model, EXO1 physically associates with MLH1 (Tran et al., 2001), promotes
124 MutLgamma nuclease activity in vitro (Cannavo et al., 2020; Kulkarni et al., 2020), and can increase the
125 stability of MLH1 containing mismatch repair complexes (Amin et al., 2001). Given that CO interference
126 is unchanged in *Exo1*$^{-/-}$ spermatocytes, we favor the latter model that lower MLH1 and MLH3 foci reflect
127 reduced stability of the MutLgamma complex in the absence of EXO1.

128 Although there are substantial MLH1/MLH3 foci in *Exo1*$^{-/-}$ spermatocytes, most of these sites do
129 not result in COs (Kan et al., 2008; Wei et al., 2003). We observed fewer bivalents per cell on average
130 in *Exo1*$^{-/-}$ (5.3 ± 2.0) as compared to *Exo1*^{het} spermatocytes (19.9 ± 0.3) (**Figure 1D**). Consistent with
131 earlier reports, *Exo1*$^{-/-}$ showed a less severe reduction in bivalents than *Mlh3*$^{-/-}$ spermatocytes (Kan et
132 al., 2008). This finding suggests that MLH3, and likely MutLgamma may be required for the majority of
133 COs in *Exo1*$^{-/-}$ spermatocytes. Consistent with this hypothesis, *Mlh3* is epistatic to *Exo1* as *Exo1*$^{-/-}$*Mlh3*$^{-}$
134 $^{/-}$ spermatocytes have similar number and distribution of bivalents per cell as that of *Mlh3*$^{-/-}$
135 spermatocytes (**Figure 1D**).

136 Variability in the number of bivalents per cell is low in spermatocytes with efficient CO
137 maturation likely reflecting strong CO assurance. For example, in WT and *Exo1*^{het} spermatocytes we
138 found Coefficents of Variation (CoVs, a ratio of the standard deviation by the mean) of 2.7% and 1.3%,

139 respectively. By contrast in *Mlh3*$^{-/-}$ and *Exo1*$^{-/-}$*Mlh3*$^{-/-}$ spermatocytes the CoVs were 84% and 96%,
140 respectively. The high cell to cell variation in the number of bivalents could reflect that SSNs do not
141 generate COs from intermediates that are subject to CO assurance mechanisms. However, we found
142 that 2/3 of COs in *Mlh3*$^{-/-}$ spermatocytes require RNF212, suggesting that they largely derive from CO
143 designated and assured intermediates ((Reynolds et al., 2013) and R.K, F.C., unpublished data).
144 Instead, the high variability of bivalents per cell likely reflects variability in the number of intermediates
145 or in the number of intermediates that can be acted upon by SSNs. We favor the latter model as yeast
146 lacking Mlh3 have wild-type levels of joint molecules (Arter et al., 2018; De Muyt et al., 2012;
147 Zakharyevich et al., 2012), overall recombination activity is similar between WT, *Mlh3*$^{-/-}$, and *Exo1*$^{-/-}$
148 spermatocytes (**Figure S1B**), and because CO interference is unchanged in *Exo1*$^{-/-}$ spermatocytes
149 (**Figure S1C**). Given this model, it is interesting that we find an intermediate CoV for bivalents per cell
150 in *Exo1*$^{-/-}$ spermatocytes of 39.1% (**Figure 1D**), suggesting a large fraction of these COs may derive
151 from SSNs contradicting the simple hypothesis that most COs in *Exo1*$^{-/-}$ spermatocytes are
152 MutLgamma-derived.
153

154 ***Exo1*$^{-/-}$ COs are dependent upon MLH3 and independent of EXO1 nuclease activity**

155 To definitively determine the roles of EXO1 in CO formation, we compared recombination
156 outcomes between mutants at the *59.5* hotspot on Chr19. Spermatocytes lacking COs apoptose at
157 metaphase I causing azoospermia and infertility. To directly compare mutants with WT, we isolated
158 spermatocytes at the end of meiotic prophase I (Late 4C). In WT sperm, we find that 67% of
159 recombinants at *59.5* are COs (Zelazowski et al., 2017) (**Table 1, Figure S1B**). The remaining
160 recombinants are singletons, NCO gene conversions that include only one polymorphism (29%) and
161 co-conversions, NCO gene conversions that include two or more polymorphisms (4%). In support of our
162 experimental approach, recombination outcomes are equivalent between sperm and isolated diplotene
163 spermatocytes in WT (**Figure S1B**).

164 To determine the contribution of EXO1-dependent nuclease activity to crossing over, we
165 compared recombination between *Exo1*$^{-/-}$ spermatocytes and a nuclease-deficient allele (*Exo1*nd) that
166 replaces one of the five metal binding residues (D173A) and reduces nuclease activity by at least 98%
167 in vitro (Myler et al., 2016; Shao et al., 2014; Sokolsky and Alani, 2000; Tran et al., 2002; Wang et al.,
168 2022; Zhao et al., 2018). *Exo1*^{het} and *Exo1*$^{nd/nd}$ spermatocytes showed 28% lower CO frequencies than
169 WT spermatocytes at *59.5* (**Figure 2A**). However both *Exo1*^{het} and *Exo1*$^{nd/nd}$ mice are fertile and global
170 bivalents in metaphase are similar between *Exo1*^{het} and WT spermatocytes (Wang et al., 2022) (**Figure**
171 **1D**). It is possible that in-depth analysis of recombination at *59.5* may reveal subtle haploinsufficient
172 phenotypes for EXO1. To increase rigor, we limited any comparisons of *Exo1*$^{-/-}$ spermatocytes to
173 *Exo1*^{het}. *Exo1*$^{-/-}$ spermatocytes received 77.9% fewer COs compared to *Exo1*^{het} (**Figure 2A, Table 1**),
174 similar to the 73.4% fewer COs observed globally (**Figure 1D**) and supporting the concept that in depth
175 analysis of *59.5* can reflect general recombination mechanisms. As expected from previous reports
176 (Keelagher et al., 2011; Zakharyevich et al., 2010), this CO defect was not seen in *Exo1*$^{nd/nd}$ mice
177 (Wang et al., 2022) (**Figure 2A, Table 1**) and they are fertile (Zhao et al., 2018). Taken together, these
178 findings suggest the CO role of EXO1 in mice is nuclease-independent globally and at *59.5*.
179 *Exo1*$^{-/-}$ had 91-fold higher COs at *59.5* compared to *Mlh3*$^{-/-}$ spermatocytes (**Figure 2A**). Similar
180 to the genetic dependence for global crossing over, *Mlh3* was epistatic to *Exo1* for COs at *59.5* as
181 *Exo1*$^{-/-}$*Mlh3*$^{-/-}$ spermatocytes had similar CO frequency to *Mlh3*$^{-/-}$ (**Figure 2A, Table 1**). Taken together,
182 COs in *Exo1*$^{-/-}$ spermatocytes require MLH3 and are independent of EXO1 nuclease activity.
183

184 **COs in *Exo1*$^{-/-}$ spermatocytes are more complex and show altered breakpoints**

185 Most COs observed in WT and mutant spermatocytes show a single exchange point between
186 parental haplotypes (simple COs) (**Figure 2B)**. However, we occasionally see COs that involve a
187 contiguous tract that scores positive for both parental haplotypes. We refer to these as 'mixed COs' as
188 the simplest interpretation is that these samples contain two independent simple COs that have
189 different exchange points. In support of this interpretation, the number of mixed COs was not

190 significantly different from the number of samples predicted to have multiple COs by Poisson
191 approximation and the frequency of mixed COs is lower when fewer input molecules are used. We can
192 observe complex COs with more than two haplotype switches that may involve tracts that are positive
193 for both parental haplotypes. These complex COs cannot be explained as multiple events, but are likely
194 caused by template switches or branch migration during CO formation and/or mismatch repair. These
195 events are rare in WT spermatocytes or sperm (0.4 ± 0.9% and 2.5 ± 3.5%, respectively), however
196 complex COs were more frequently seen in spermatocytes lacking EXO1 (32.4 ± 24.1%) (**Figure 2B)**.
197 EXO1-dependent mismatch correction predominantly requires EXO1's nuclease function (Goellner et
198 al., 2015; Wang et al., 2022). In order to determine the contribution to complex COs from defective
199 mismatch repair, we compared *Exo1*$^{-/-}$ and *Exo1*$^{nd/nd}$ spermatocytes (**Figure 2B**). We observed fewer
200 complex COs in *Exo1*$^{nd/nd}$ spermatocytes (14.4 ± 9.7%). Together, the higher frequency of complex
201 COs seen in *Exo1*$^{-/-}$ spermatocytes likely reflects both nuclease-dependent and -independent roles of
202 EXO1, implying that template switching/branch migration is likely more frequent in *Exo1*$^{-/-}$ COs than that
203 of *Exo1*$^{nd/nd}$ and WT.

204 Most meiotic DSBs at the *59.5* hotspot in a BxD F1 hybrid occur on the B chromosome. As
205 such, most of the CO-dependent gene conversions alter the recipient B chromosome in favor of the
206 donor D chromosome. As a consequence CO breakpoint distributions show reciprocal CO asymmetry
207 (Jeffreys and Neumann, 2002; Zelazowski et al., 2017) (**Figure 2C**). The majority of B (recipient) to D
208 (donor) CO breakpoints cluster to the left of the hotspot center (Top, red) and the majority of D to B
209 breakpoints cluster to the right (Bottom, blue). Additionally, the distance between the midlines of the
210 two CO breakpoint distributions reflects the average CO-dependent gene conversion tract. The
211 estimated gene conversion tract length observed in *Exo1*^{het} and *Exo1*$^{nd/nd}$ spermatocytes was ~400bp
212 similar to that of WT (**Figure 2C**) (Zelazowski et al., 2017). However, we observed that *Exo1*$^{-/-}$
213 spermatocytes had a lower estimated gene conversion tract length of 182bp. As *Exo1*$^{nd/nd}$
214 spermatocytes have similar estimated gene conversion tract length as *Exo1*^{het}, it is unlikely that
215 defective mismatch repair in *Exo1*$^{-/-}$ contributes to this phenotype.

This decrease in estimated gene conversion tract length in *Exo1*$^{-/-}$ spermatocytes may be caused by a decrease in the proportion of DSBs or CO designations on the B vs D homolog. However, we see 2.3- and 2.0-fold more NCOs on the B versus D chromosome in *Exo1*$^{-/-}$ and *Exo1*^{het} spermatocytes, respectively, consistent with similarly high DSBs on B in both genotypes, and we still see reciprocal CO asymmetry in *Exo1*$^{-/-}$ spermatocytes despite the shorter apparent gene conversion tract. It is also possible that *Exo1*$^{-/-}$ spermatocytes have shorter CO-dependent gene conversions, however this should correlate with the length of all recombination outcomes derived from the designated CO intermediate and we do not see this (described below). Instead we favor a model that there is non-stereotypical positioning of CO breakpoints in *Exo1*$^{-/-}$ spermatocytes because we observe many CO breakpoints accumulating towards the center of the hotspot, where we rarely see breakpoints in *Exo1*^{het} and *Exo1*$^{nd/nd}$ spermatocytes ($p = 0.0005$ and 0.0416, respectively Fishers Exact test, two-tailed, **Figure 2C**). The enrichment of CO breakpoints in the center of the hotspot may reflect altered branch migration of the double Holliday junction intermediate in *Exo1*$^{-/-}$ spermatocytes. In support of this model, the inferred positions of Holliday junctions are altered in budding yeast in the absence of MutLgamma or Exo1 (Marsolier-Kergoat et al., 2018). Alternatively the enrichment may be driven by differences in the endonucleolytic behavior of CO resolving enzymes.

Most COs in *Exo1*$^{-/-}$ spermatocytes are derived from SSNs

Exo1$^{-/-}$ spermatocytes show higher CO levels than *Mlh3*$^{-/-}$, both locally at *59.5* and globally in metaphase bivalents, and all these COs require MLH3 (**Figure 1D, 2A**), suggesting they derive from residual MutLgamma cleavage. Counterintuitively, the CoV of bivalent numbers per cell in *Exo1*$^{-/-}$ spermatocytes support a model that COs in *Exo1*$^{-/-}$ may arise via enzymatic activity of SSNs. A cohesive interpretation of these disparate findings could be that the residual COs in *Exo1*$^{-/-}$ spermatocytes require MutLgamma structurally, but not enzymatically. If so, we would expect COs in *Exo1*$^{-/-}$ spermatocytes to share features with COs from a nuclease-dead allele of *Mlh3* (*Mlh3*$^{DN/DN}$) that

241 replaces a conserved active site residue (D1185N) and eliminates MutLgamma endonuclease activity
242 in vivo and vitro (Nishant et al., 2008; Raghavan, 2019; Toledo et al., 2019).
243 In *Mlh3*$^{DN/DN}$ spermatocytes, MLH1, MLH3, CDK2, and HEI10 form foci with similar timing,
244 frequency, and distribution as WT (Toledo et al., 2019). However, like *Exo1*$^{-/-}$, most of these
245 MutLgamma associated sites fail to become COs. We saw that *Mlh3*$^{DN/DN}$ spermatocytes had 5.5 ± 1.9
246 bivalents per cell on average, like *Exo1*$^{-/-}$ (5.3 ± 2.0), but significantly more than *Mlh3*$^{-/-}$ (1.4 ± 1.1)
247 (**Figure 3**). Additionally, bivalent distribution was similar between *Mlh3*$^{DN/DN}$ and *Exo1*$^{-/-}$ with CoVs of
248 34.7% and 39.1%, respectively. MutLgamma containing *Mlh3*$^{DN/DN}$ lacks endonuclease activity (Nishant
249 et al., 2008; Raghavan, 2019; Toledo et al., 2019) suggesting the residual COs seen here are likely
250 derived from SSNs. Consistently, it was previously reported that chiasmata number in *Mlh3*$^{-/-}$ and
251 *Mlh3*$^{DN/DN}$ spermatocytes partially require MUS81, one of several SSNs (Holloway et al., 2008; Toledo
252 et al., 2019). We find that spermatocytes lacking MUS81 are fertile and show a WT level of bivalents as
253 expected, but that *Mus81*$^{-/-}$*Exo1*$^{-/-}$ spermatocytes had only 4.1 ± 1.9 bivalents per cell, significantly
254 fewer than *Exo1*$^{-/-}$, providing support for the model that the residual COs in *Exo1*$^{-/-}$ and *Mlh3*$^{DN/DN}$ are
255 derived from SSNs. Taken together, we suggest that residual COs in *Exo1*$^{-/-}$ may be independent of
256 MutLgamma endonuclease activity, but dependent upon MutLgamma structurally. In support of MLH3's
257 structural role, the number of bivalents in *Mlh3*^{DN} were dosage sensitive as we saw fewer bivalents per
258 cell on average in *Mlh3*$^{-/DN}$ (3.97 ± 1.9) as compared to *Mlh3*$^{DN/DN}$ spermatocytes (**Figure 3**). Dosage
259 sensitivity is more consistent with a structural rather than an enzymatic function. Further, we suggest
260 that this structural role of MLH3 must be upstream of EXO1 given the epistatic relationship between
261 *Mlh3*$^{-/-}$ and *Exo1*$^{-/-}$.
262 To determine when recombination outcomes form in these CO-defective mutants, we
263 synchronized spermatogenesis to enrich for specific stages of meiotic prophase (**Figure 4A**, see **Table**
264 **S1** for sample purity). We found that in WT, MLH3-derived COs appear during pachynema, while in
265 *Mlh3*$^{-/-}$, SSN-derived COs appear during diplonema (**Figure 4B**). Given the temporal separation
266 between MLH3-dependent and -independent COs, we sought to determine when the residual *Exo1*$^{-/-}$

267 COs appear. We saw that 60% of COs in *Exo1*$^{-/-}$ spermatocytes are detectible in diplonema, suggesting
268 the majority of residual COs derive from SSNs (**Figure 4B**). Additionally, we find that residual CO levels
269 at *59.5* are similar between *Mlh3*$^{DN/DN}$ and *Exo1*$^{-/-}$ Late 4C and diplotene spermatocytes (19.9 ± 9.0,
270 25.6 ± 7.3, and 22.7 ± 10.8, respectively) (**Table 1**), suggesting the residual COs in *Exo1*$^{-/-}$ may be
271 independent of MLH3 nuclease activity. While it is possible that *Mlh3*$^{DN/DN}$ and *Exo1*$^{-/-}$ have similar
272 numbers of residual COs by coincidence, MutLgamma COs fully require Exo1 in budding yeast
273 (Argueso et al., 2004; Gioia et al., 2021; Nishant et al., 2008; Zakharyevich et al., 2010). We favor a
274 more cohesive model that most residual COs in *Exo1*$^{-/-}$ are derived from SSNs and that MutLgamma
275 nuclease activity is heavily reliant on EXO1 in mouse spermatocytes.
276

277 **Alternative DNA repair outcomes in *Exo1*$^{-/-}$ spermatocytes appear in diplonema**

278 Due to the preponderance of COs at *59.5*, we observe a high frequency of co-conversions in
279 spermatocytes defective for CO maturation, such as *Mlh3*$^{-/-}$ and *Hei10*$^{-/-}$ (**Figure S1B, Table 1**). We
280 have previously shown that in *Mlh3*$^{-/-}$ spermatocytes, these co-conversions likely arise via SDSA and/or
281 dissolution of CO designated intermediates (Zelazowski et al., 2017). In support of this model, we only
282 see enrichment of co-conversions on the B (recipient) chromosome on which we find most CO-
283 dependent gene conversion and never on the D (donor) chromosome as would be expected from SSN-
284 dependent resolution (Marsolier-Kergoat et al., 2018). Finally, we see no enrichment of co-conversions
285 in mutants lacking CO designation such as *Rnf212*$^{-/-}$ (**Figure S1B** and L.P, F.C unpublished data). To
286 determine when these co-conversions form, we examined recombination in synchronized *Exo1*$^{-/-}$
287 compared to WT and *Mlh3*$^{-/-}$ spermatocytes (**Figure 4C, Table 1**). In WT, co-conversions form at a low
288 frequency in pachynema and we do not see an increase in diplonema. *Mlh3*$^{-/-}$ and *Exo1*$^{-/-}$
289 spermatocytes have similarly low frequencies of co-conversions in pachynema as WT frequencies at all
290 stages. Whereas in diplonema, *Mlh3*$^{-/-}$ spermatocytes had 10-fold more co-conversions than in
291 pachynema, as well as 13- and 6-fold more co-conversions as WT diplonema and sperm, respectively
292 (**Figure 4C, 5A**). Similarly, *Exo1*$^{-/-}$ had 5-fold more co-conversions in diplonema than pachynema, and

293 10- and 5-fold more co-conversions in diplonema than WT spermatocytes and sperm, respectively. We
294 suggest that the co-conversions in *Exo1*$^{-/-}$ and *Mlh3*$^{-/-}$ spermatocytes are products of back-up repair
295 pathways acting on unrepaired CO-designated intermediates in diplonema or during the pachynema to
296 diplonema transition. Intriguingly, despite the high levels of SDSA leading to NCOs in pachynema
297 (**Table 1**), CO intermediates appear inaccessible to SDSA. We find that if CO intermediates are
298 designated, they can only be resolved by MutLgamma in pachynema or repaired by back-up pathways
299 later.
300

301 **Co-conversion length in CO defective mutants suggests additional steps in CO intermediate**
302 **processing**

303 Having established that *Exo1*$^{-/-}$ co-conversions at *59.5* likely arise from back-up repair pathways
304 acting after pachynema, we sought to define the features of these co-conversions. The lengths, degree
305 of discontinuity, genetic dependence, and distribution of these co-conversions should reflect
306 characteristics of the CO designated intermediates from which they are derived providing mechanistic
307 insight. For example, co-conversions that form during diplonema in CO maturation mutants should be
308 longer than those that arise via SDSA in pachynema. Consistent with this concept, we saw that co-
309 conversions in *Mlh3*$^{-/-}$ and *Exo1*$^{-/-}$ pachytene spermatocytes were 190 ± 157bp and 223 ± 105bp long,
310 respectively (**Figure 5B,** R.K., F.C. unpublished data) and were similar in length to each other and
311 those isolated from WT pachynema and diplonema, suggesting that they arise from similar
312 intermediates and likely via SDSA. By contrast, co-conversions detected in *Mlh3*$^{-/-}$ and *Exo1*$^{-/-}$ diplotene
313 spermatocytes averaged 427 ± 239bp and 813 ± 511bp, respectively, and were significantly longer than
314 co-conversions from their pachytene counterparts or WT spermatocytes. Curiously, we saw that co-
315 conversions from *Exo1*$^{-/-}$ diplotene spermatocytes were significantly longer than those from *Mlh3*$^{-/-}$
316 (**Figure 5A, B**). Considering that the co-conversion tract length likely reflects its precursor intermediate,
317 we suggest that the CO designated precursor elongates in *Exo1*$^{-/-}$, a process that may require MLH3.
318

319 **Elongated co-conversions in *Exo1*$^{-/-}$ spermatocytes require MLH3 structurally**

320 To definitively determine the genetic dependence of the frequency, distribution, and length of
321 co-conversions, we analyzed NCOs in multiple CO maturation mutants and double mutants. Similar to
322 observations in diplonema, we saw that co-conversions isolated from Late 4C *Exo1*$^{-/-}$ spermatocytes
323 were longer (692 ± 567bp) than those isolated from *Mlh3*$^{-/-}$ (298 ± 231bp) (**Figure 5C**). We also saw
324 that co-converted NCOs from *Exo1*$^{-/-}$*Mlh3*$^{-/-}$ spermatocytes were similar in length (334 ± 288bp) to those
325 isolated from *Mlh3*$^{-/-}$. As such, MLH3 is required for the elongated co-conversions seen in the absence
326 of EXO1. Generally, *Exo1*$^{-/-}$ has a stronger mismatch correction defect than MutLgamma (Furman et al.,
327 2021), likely ruling out defective mismatch repair as a significant contributor to elongation of the co-
328 conversions seen in *Exo1*$^{-/-}$ spermatocytes. Further supporting this premise, we found that co-
329 conversions isolated from *Exo1*$^{-/-}$*Msh2*$^{-/-}$ were not significantly changed in length (1111 ± 898bp) to
330 those from *Exo1*$^{-/-}$ spermatocytes. Elongation of co-conversions in *Exo1*$^{-/-}$ spermatocytes was
331 independent of MUS81, supporting our model that co-conversions likely result from dissolution or
332 SDSA-like mechanisms, rather than from double Holliday junction resolution, although we cannot rule
333 out that redundant SSN pathways play a role. We suggest elongation of the designated CO precursor
334 leads to elongation of the co-conversions in *Exo1*$^{-/-}$, *Exo1*$^{-/-}$*Msh2*$^{-/-}$, and *Exo1*$^{-/-}$*Mus81*$^{-/-}$ as compared to
335 *Mlh3*$^{-/-}$ or *Exo1*$^{-/-}$*Mlh3*$^{-/-}$ spermatocytes.

336 A major difference between the mutants with shorter and longer co-conversions is that
337 MutLgamma accumulates at CO sites in *Exo1*$^{-/-}$, *Exo1*$^{-/-}$*Msh2*$^{-/-}$, and *Exo1*$^{-/-}$*Mus81*$^{-/-}$ spermatocytes
338 (**Figure 1C)** (Kan et al., 2008; Wei et al., 2003). Therefore, we sought to test whether MutLgamma
339 focus formation is required to observe elongation of co-conversions and of the inferred designated CO
340 intermediate. We analyzed NCO frequency and distribution in *Hei10*$^{-/-}$ and *Hfm1*$^{-/-}$ spermatocytes. In
341 mouse spermatocytes, HEI10 is proposed to target MutSgamma for ubiquitination and degradation
342 allowing exchange in favor of MutLgamma at designated CO sites (Qiao et al., 2014; Rao et al., 2017;
343 Ward et al., 2007). HFM1 is a Mer3 helicase ortholog and is required for full synapsis, formation of
344 MutLgamma foci at CO sites, and 80% of chiasmata in mouse spermatocytes (Guiraldelli et al., 2013).

345 As such, MLH1 and MLH3 are present in *Hei10*$^{-/-}$ and *Hfm1*$^{-/-}$ spermatocytes, but do not form
346 MutLgamma foci on CO sites. In *Hfm1*$^{-/-}$ and *Hei10*$^{-/-}$, co-conversions were similar in length (347 ±
347 167bp, 329 ± 231bp, respectively) to co-conversions from Late 4C *Mlh3*$^{-/-}$ spermatocytes (**Figure 5C**).
348 We infer that the presence of MLH3 alone is insufficient to elongate the co-conversions. Additionally,
349 the similar level of co-conversions found in *Hfm1*$^{-/-}$ compared to *Mlh3*$^{-/-}$ spermatocytes suggests that
350 unlike yeast Mer3 (Borner et al., 2004), HFM1 is not required for CO designation.
351 To test if MutLgamma focus formation correlates with longer co-conversions, we analyzed
352 *Mlh3*$^{DN/DN}$ spermatocytes. Similar to *Exo1*$^{-/-}$, the *Mlh3*$^{DN/DN}$ allele is defective for CO maturation, but is
353 proficient for MutLgamma focus formation at likely designated CO sites (Toledo et al., 2019).
354 Interestingly, we observed that co-conversions from *Mlh3*$^{DN/DN}$ and *Mlh3*$^{-/DN}$ (619 ± 422bp and 613 ±
355 432bp, respectively) were similar in length to co-conversions from *Exo1*$^{-/-}$ and significantly longer than
356 those from *Mlh3*$^{-/-}$ spermatocytes (**Figure 5C**). Indirect estimations and direct measurements show that
357 CO gene conversion tract lengths in mice and humans are ~600 bp at multiple hotspots (Cole et al.,
358 2014; Jeffreys and Neumann, 2002; Zelazowski et al., 2017). Comparing the co-conversions across
359 multiple mutants, we observe that those with MutLgamma foci have longer gene conversion tracts than
360 those without, and that the longer tracts resemble mammalian CO-dependent gene conversion (**Figure**
361 **5C**). We suggest that the CO precursor intermediate has further differentiated in mutants that load
362 MutLgamma on the axes. In support of this concept, there are more SSN-derived bivalents in *Exo1*$^{-/-}$
363 and *Mlh3*$^{DN/DN}$ suggesting the precursor intermediate may have progressed further towards CO
364 maturation capability (**Figure 3**). We suggest this progression also occurs in wild type upon association
365 of MutLgamma, but is rapidly resolved as a CO because MLH3 is proficient for nuclease activity. Taken
366 together, the inferred elongation of the designated CO intermediate is associated with MutLgamma
367 focus formation, independent of MLH3 nuclease activity, and correlates with increased probability of
368 resolution as a CO.
369

370 **Co-conversions from *Exo1*$^{-/-}$ and *Mlh3*$^{DN/DN}$ are frequently discontinuous**

371 Discontinuous co-conversions involve a single event that has four genotype switches between parental
372 haplotypes (e.g., asterisks, **Figure 5A**). An apparent discontinuous co-conversion could arise from two
373 independent NCOs occurring in the same samples. Indeed, the number of discontinuous co-
374 conversions that involved a singleton and a contiguous co-conversion were found at the frequency
375 predicted by Poisson approximation for multiple events per sample. As such, these events were
376 removed from the analysis (Supplementary data file). By contrast, the number of discontinuous co-
377 conversions that involved two separate contiguous co-converted tracts were much higher than
378 predicted by Poisson. On average a greater fraction of co-conversions were discontinuous in *Exo1*$^{-/-}$
379 (19.4 ± 23.9%) as compared to *Mlh3*$^{-/-}$ spermatocytes (0.8 ± 3.9%) (**Figure 5D**). This 24-fold higher
380 frequency of discontinuity cannot be explained by the ~2-fold longer co-conversion tract length between
381 *Mlh3*$^{-/-}$ and *Exo1*$^{-/-}$ spermatocytes. Discontinuity may involve defects in mismatch repair, as expected
382 based on the role of EXO1 in MLH1-dependent MutLalpha activity. Consistent with this premise, levels
383 of discontinuity were similar between *Exo1*$^{-/-}$ and *Msh2*$^{-/-}$*Exo1*$^{-/-}$ (21.5 ± 11.7%), suggesting absence of
384 EXO1 alone is sufficient for this phenotype. Loss of MUS81 does not influence the frequency or
385 discontinuity of co-conversions consistent with their formation likely arising from dissolution and SDSA-
386 like mechanisms. Interestingly, we saw that *Mlh3*$^{-/-}$*Exo1*$^{-/-}$ has an intermediate phenotype with the
387 fraction of discontinuous co-conversions (5.3 ± 6.8%) being significantly different from both *Mlh3*$^{-/-}$ and
388 *Exo1*$^{-/-}$ (**Figure 5D**). Discontinuity of co-conversions is the only phenotype for which *Mlh3* is not epistatic
389 to *Exo1*, supporting the interpretation that mismatch repair plays at least a partial role in formation of
390 discontinuos co-conversions. Not exclusively, discontinuity could reflect template switching in the
391 formation of the elongated CO intermediate. In support of this model, co-conversions in *Mlh3*$^{-/DN}$ had a
392 high fraction of discontinuity (14.6 ± 6.6%), suggesting either template switching and/or lack of efficient
393 mismatch repair. Similarly, co-conversions in *Mlh3*$^{DN/DN}$ were also discontinuous (9.5 ± 11.8 %),
394 however there were too few events for analysis. Perhaps the presence of nuclease-dead MLH3 may
395 impede MLH1 function in MutLalpha mismatch repair in this context. However, template switching is
396 frequently observed in budding yeast lacking MLH3 or EXO1 (Marsolier-Kergoat et al., 2018), and has

397 been proposed to occur frequently during CO formation (Ahuja et al., 2021). We favor the model that
398 defects in mismatch repair contribute to discontinuity, but the lion's share is owing to template switching
399 upon elongation of the designated CO intermediate. In support of this model, we find a similar fraction
400 of discontinuos COs and co-conversions in *Exo1*$^{-/-}$ (**Figure 2B**). Further, we see a two-fold higher
401 frequency of discontinuous COs in *Exo1*$^{-/-}$ than in *Exo1*$^{nd/nd}$ spermatocytes, suggesting additional
402 mechanisms contribute to discontinuity than defective mismatch repair. Importantly, when MLH3 retains
403 its EXO1-dependent nuclease activity, discontinuity is not apparent, suggesting that the MutLgamma
404 nicking to resolve COs also contributes to conversion or reversion of mismatches as predicted in yeast
405 and previously suggested in mouse spermatocytes (Peterson et al., 2020).
406

407 **Both 3' ends of a DSB are equally likely to invade and polymerize from the homolog at *59.5***

408 In order to glean any evidence for how the CO-designated intermediate is formed and differentiated, we
409 analyzed the distribution of co-conversions in the two classes of CO maturation mutants (*Mlh3*$^{-/-}$-like
410 and *Exo1*$^{-/-}$-like). Importantly, *59.5* is an asymmetric hotspot in the BxD F1 hybrid and experiences a
411 higher frequency of SPO11-dependent DSBs on the B rather than the D chromosome. The majority of
412 these DSBs occur directly at the hotspot center (**Figure 5A**) (Lange et al., 2016) (marked with a dashed
413 line and plotted at 0kb throughout), where a polymorphism confers a high affinity PRDM9 binding site
414 on the B chromosome that specifies the *59.5* hotspot. Consistent with the differential break frequency
415 between homologs, there is a concomitant three-fold higher frequency of NCOs in WT on the B versus
416 D chromosome and reciprocal CO asymmetry (Zelazowski et al., 2017). Intriguingly, the long co-
417 conversions seen in *Mlh3*$^{-/-}$-like and *Exo1*$^{-/-}$-like mutants are found exclusively on the B chromosome,
418 suggesting that only DSBs initiated on B are capable of becoming designated CO sites. The asymmetry
419 of meiotic DSBs at *59.5* and the subsequent asymmetry of the resulting co-conversions provides an
420 opportunity to investigate whether any strand invasion or extension biases can be inferred about the
421 CO-designated intermediate based upon the distribution of co-conversions.

422 We categorized the co-conversions as to whether they were to the left, spanning, or to the right
423 of the hospot center (**Figure 5E, top**). In examining the co-conversion distribution, it would appear that
424 there is a marked enrichment for co-conversions on the "right" side of the hotspot center (**Figure 5A,**
425 dotted line). For example, in *Mlh3*$^{-/-}$ we find 100 co-conversions to the right and only 16 to the left
426 (**Figure 5E**). This right-sided enrichment was present in all mutants, but was particularly prevalent in
427 mutants of the *Mlh3*$^{-/-}$-like class. This could reflect a preference for strand invasion by one end of the
428 DSB. However, the polymorphism density to the right of the hotspot center is higher than to the left
429 raising the possibility that we have more detectible events on the right side (**Figure 5F, 'Original**
430 **polymorphism location'**). To correct for the influence of polymorphism density, we mirror inverted the
431 polymorphism location at the hotspot center from left to right and determined whether the original co-
432 conversions would have been detected given the altered polymorphism map (**Figure 5F, 'Inverted**
433 **polymorphism location'**). There were four outcomes after inverting the polymorphisms and examples
434 of each are shown in **Figure 5F**: Type-1) one-sided co-conversions that would not have been detected;
435 Type-2) one-sided co-conversions that would have been detected; Type-3) co-conversions that span
436 the hotspot center originally, but would be detected as one-sided; and Type-4) co-conversions that
437 span the hotspot center originally and would remain detected as such. To counter any potential
438 detection skew, Type-1 co-conversions were removed from the analysis and Type-3 co-conversions
439 were re-scored as one-sided (**Figure 5E, bottom**). Upon this reassessment, we found no significant
440 difference between the frequency of events on either side of the hotspot center, confirming our
441 suspicion that the polymorphism density was driving the apparent right-sided enrichment. In conclusion,
442 either end of the DSB is equally likely to engage in strand invasion at *59.5*.
443

444 **Co-conversion distribution suggests step wise polymerization of 3' invaded ends**

445 One intriguing observation in the *Mlh3*$^{-/-}$-like class of mutants is that only 4% of co-conversions
446 span the hotspot center (**Figure 5A,E**). If both ends of the DSB extend via polymerization, we would
447 expect most of these co-conversions would incorporate the hotspot center, despite their relatively short

448 average length of 311bp. Therefore, we suggest that the CO-designated intermediate in the *Mlh3*$^{-/-}$-like
449 class of mutants is extended from only a single invaded 3' end. By contrast, 25% of events in the *Exo1*$^{-}$
450 $^{/-}$-like class of mutants span the hotspot center suggesting that both ends of the DSB are extended.
451 Why then don't all *Exo1*$^{-/-}$-like co-conversions span the hotspot center? These spanning co-conversions
452 show a marked skew in distribution with ~72% occuring on only one side of the hotspot resulting in a
453 long and short arm of the co-conversions (**Figure 5G**). We suggest that upon MutLgamma loading in
454 the *Exo1*$^{-/-}$-like class of mutants, the initial invaded 3' end is further extended by polymerization and the
455 second end is 3-fold less polymerized on average. The shorter extended tract on the second end would
456 frequently fail to incorporate a polymorphism such that the majority of events still appear one-sided.
457 Consistent with this premise, 40% of the spanning co-conversions in the *Exo1*$^{-/-}$-like class were
458 categorized as Type-3 outcomes upon mirror inverting polymorphisms and would have been detected
459 as one-sided (**Figure 5F**).

460 A consequence of the shorter polymerization of one 3' end in *Exo1*$^{-/-}$ would be that upon
461 resolution of this intermediate, one of the CO breakpoints should be close to the hotspot center, which
462 is what we observe in the CO breakpoint mapping (**Figure 2C**). If we plot the ends of the *Exo1*$^{-/-}$ co-
463 conversions as hypothetical CO breakpoints, we find our hypothetical CO breakpoint map is similar to
464 the observed CO break point map in *Exo1*$^{-/-}$ with similar reciprocal CO asymmetry and shorter inferred
465 gene conversion tract length (**Figure S2**). Considering the shorter single-end extended CO precursor in
466 the *Mlh3*$^{-/-}$-like mutants, we would expect the SSN dependent COs to form even closer to the hotspot
467 center than in *Exo1*$^{-/-}$ spermatocytes. Indeed, we find that 85% of COs in *Mlh3*$^{-/-}$-like mutants (12 out of
468 14) are found in the central 500bp as opposed to 54% in *Exo1*$^{-/-}$ (53 out of 98) and 32% in *Exo1*^{het} (30
469 out of 92) (0.0398 and 0.0002, respectively Fisher's exact test, two-tailed). Taken together, we suggest
470 the single-end extended intermediate is independent of MLH3, the dual-end extended intermediate is
471 dependent upon MLH3 structurally, and that both are likely formed in pachynema. In the absence of
472 MutLgamma resolvase activity, both single- and dual-end intermediates are substrates that can be
473 resolved by SSNs or dissolved after pachynema.

474 Unlike *Exo1*$^{-/-}$, in wild type, *Exo1*^{het}, and *Exo1*nd the majority of COs are simple and their
475 breakpoints show more reciprocal CO asymmetry (**Figure 2B, 2C, S2**). We surmise that when
476 MutLgamma is enzymatically proficient, retained heteroduplex and evidence of template switching is
477 less frequent and CO breakpoints are more evenly distributed away from the hotspot center. Perhaps
478 MLH3-dependent nicking can direct mismatch repair and/or strand processing during CO formation. In
479 support of this model, genomic analysis of COs in *Msh2*$^{-/-}$ budding yeast show fewer heteroduplex
480 strands as compared to those lacking Msh2 along with Mlh1, Mlh3, Exo1, or Sgs1(Marsolier-Kergoat et
481 al., 2018). Further, in depth analysis of COs at one highly polymorphic hotspot in *Msh2*$^{-/-}$ budding yeast
482 suggests frequent CO resolution-associated strand processing (Ahuja et al., 2021), and retained
483 heteroduplex is rare in *Msh2*$^{-/-}$ mouse spermatocytes (Peterson et al., 2020).
484 Taken together, we suggest that the co-conversion pattern in the *Mlh3*$^{-/-}$-like and *Exo1*$^{-/-}$-like
485 class of mutants reflects two independent DNA repair intermediates (**Figure 6**). First a single end
486 invades and extends ~300bp to form an extended single-end invasion intermediate (eSEI), this
487 relatively stable intermediate requires MutLgamma to be loaded on the axis for the second end to be
488 captured forming a nicked double Holliday junction. Both ends are extended by polymerization, but the
489 second end polymerizes to a shorter extent. Alternatively, second end capture could occur prior to
490 MutLgamma loading with minimal or no extension occuring on the second end. Finally, MutLgamma
491 nicking directs strand processing and mismatch repair to reorient the gene conversion tract on either
492 side of the hotspot center.
493
494 **Conclusions**
495 While many of the meiotic recombination mechanisms are conserved between budding yeast and
496 mammals, there are unique differences that provide opportunities to refine recombination models. To
497 that end, recombination analysis has been done in mouse spermatocytes in WT and a few mutants
498 (*Msh2*, *Mlh1*, and *Mlh3*) (Baudat and de Massy, 2007; Cole et al., 2014; Cole et al., 2010; Guillon et al.,
499 2005; Guillon and de Massy, 2002; Peterson et al., 2020; Svetlanov et al., 2008; Zelazowski et al.,

500 2017). Unexpectedly, mismatch defective mouse spermatocytes retain far less heteroduplex strands as
501 compared to mismatch defective yeast (Ahuja et al., 2021; Marsolier-Kergoat et al., 2018; Peterson et
502 al., 2020). Additionally, physical detection of CO precursors hasn't been accomplished in mammals. As
503 a result, we are relatively ignorant of the structure of the CO intermediates in mammals. To overcome
504 these limitations, we analyzed ~1 million haploid genome equivalents from 12 independent genetic
505 conditions at a highly polymorphic native recombination hotspot. We also determined when
506 recombination is executed in wild type and 2 mutants, and together analyzed ~1600 COs and ~4400
507 NCOs. We verify conservation of several aspects of meiotic recombination between yeast and mouse
508 spermatocytes, including several recently discovered features:

509 1) Similar to previous observations (Kirkpatrick et al., 2000), we provide evidence that EXO1
510 nuclease activity contributes to mismatch correction during meiotic recombination (**Figure 2B**).
511 2) EXO1 structurally promotes MLH3-dependent nuclease function and thereby CO formation in
512 mammals (**Figure 2A**) (Yamada et al., 2020; Zhao et al., 2018), as was first established in
513 budding yeast (Argueso et al., 2004; Gioia et al., 2021; Nishant et al., 2008; Zakharyevich et al.,
514 2010) and verified in mouse (Wang et al., 2022).
515 3) The inferred CO precursor in mutants that lack MutLgamma foci (*Mlh3*$^{-/-}$-like) is asymmetric
516 regarding the two 3' ends of the DSB, independent of MutLgamma (**Figure 5**), but dependent on
517 the ZMM protein RNF212 (**Figure S1** and R.K., F.C. unpublished data). We suggest this
518 intermediate is likely a single-end invasion intermediate – the first CO-specific precursor that is
519 physically detectible in yeast (Hunter and Kleckner, 2001).
520 4) COs and co-conversions derived from CO precursors in mutants that lack MLH3's enzymatic
521 activity (*Exo1*$^{-/-}$-like) frequently display signatures of template switching and/or branch migration
522 (**Figure 2B, 5D**), similar to recent findings based upon heteroduplex retention in *Msh2*$^{-/-}$ budding
523 yeast (Ahuja et al., 2021; Marsolier-Kergoat et al., 2018). Further, we saw evidence that MLH3's
524 nuclease activity directs substantial mismatch correction during CO formation as was previously
525 proposed (Marsolier-Kergoat et al., 2018).

526 5) We did not see evidence to support the presence of ligated dHJs in pachynema, which should
527 be amplifiable in our assays (**Figure 4C**). While absence of evidence is not evidence of
528 absence, we favor the model that dHJs are likely nicked, which has been proposed by others.
529 Resolution of nicked dHJs is compatible with the biochemical properties of MutLgamma in vitro
530 as well as the heteroduplex patterns and electron microscopy analysis in budding yeast (Bell
531 and Byers, 1983; Cannavo et al., 2020; Crown et al., 2014; Gioia et al., 2021; Kulkarni et al.,
532 2020; Manhart et al., 2017; Marsolier-Kergoat et al., 2018; Peterson et al., 2020; Stahl et al.,
533 2004)

534 We also elaborate on and provide support for models based upon observations in mouse
535 spermatocytes:

536 1) In marked contrast to budding yeast, we confirm by cytological and recombination analysis that
537 the CO phenotype in *Exo1*$^{-/-}$ spermatocytes is unlike *Mlh3*$^{-/-}$ in mouse (Kan et al., 2008; Wei et
538 al., 2003) (**Figure 1, 2A**).
539 2) There are mild alterations in the frequency of recombination intermediate foci in spermatocytes
540 lacking EXO1 (Kan et al., 2008) (**Figure 1B, C**).
541 3) We provide evidence that MUS81 contributes to residual CO formation when MutLgamma lacks
542 endonuclease activity, such as in the absence of EXO1 (**Figure 3**), as is known in budding
543 yeast and mouse (Argueso et al., 2004; Gioia et al., 2021; Holloway et al., 2014; Nishant et al.,
544 2008; Toledo et al., 2019).
545 4) A structural role that promotes SSN activity was proposed for MLH3 based upon the frequency
546 of chiasmata in *Mlh3*$^{DN/DN}$ spermatocytes (Toledo et al., 2019). We provide strong support for
547 the model that MLH3 has a nuclease-independent role (**Figure 3, 4**) that results in increased
548 COs derived from SSNs.

549 Finally, this work has expanded our understanding of mammalian meiotic recombination by inferring
550 two independent CO precursors, their genetic dependence, and identifying unique roles for CO
551 maturation proteins to establish that:

552 1) In contrast to budding yeast, in mouse spermatocytes, loss of EXO1 does not alter CO
553 interference (**Figure S1C**) nor is the Mer3 ortholog HFM1 required for CO designation (**Figure**
554 **5C, D, E and S3**).
555 2) While like budding yeast, MutLgamma-derived COs require EXO1 structurally, we establish that
556 in mouse spermatocytes, residual COs in *Exo1*$^{-/-}$ require MLH3 structurally (**Figure 3, 4B**). This
557 unexpected structural role of MLH3 is upstream and independent of EXO1.
558 3) We establish independent genetic requirements for the two 3' ends of the DSB to polymerize,
559 suggesting stepwise differentiation of CO precursors into dHJs in mouse spermatocytes.
560 Polymerization of the initial invading 3' end is independent of MutLgamma, while the structural
561 role of MLH3 promotes either second-end capture and/or polymerization from the second 3'
562 end (**Figure 5**). This in marked contrast to budding yeast, where dHJs form at similar
563 frequencies in the presence or absence of MutLgamma (Zakharyevich et al., 2010;
564 Zakharyevich et al., 2012).
565 4) MLH3's structural role likely promotes formation of dHJs with asymmetric polymerization of the
566 two invaded 3' ends (**Figure 5G**) and MLH3's nuclease role subsequently generates simple CO
567 break points that are evenly distributed around the hotspot center likely due to nick-directed
568 MMR (**Figure 5D**). Unlike MutLgamma, SSNs do not reposition CO breakpoints upon resolution
569 (**Figure S2**).
570 5) The similarities within and differences between the *Mlh3*$^{-/-}$*-like* and *Exo1*$^{-/-}$*-like* class of mutants
571 suggests that the MutLgamma-independent and MLH3 structure-dependent CO precursors are
572 stable and stereotypic, suggesting the existence of both single-end invasion and nicked-dHJ
573 intermediates in CO formation in mammals (**Figure 5, 6**).
574
575 Whole-genome analysis of CO resolution patterns in budding yeast shows that when MutLgamma is
576 proficient, there are two types of resolution biases: CO-biased resolution of dHJs and a likely
577 independent orientation bias for dHJ resolution that generates a single tract of heteroduplex with no

578 intervening fully converted tracts (Pattern 1) (Marsolier-Kergoat et al., 2018). Heteroduplex patterns at
579 specific hotspots suggests that Pattern 1 COs predominate in mouse spermatocytes as well (Peterson
580 et al., 2020). It is likely that these two resolution biases are rooted in independent asymmetries of the
581 CO precursor intermediate. Indeed we find two such asymmetries: 1) a MutLgamma-independent
582 asymmetry, where only one of the two 3' strands polymerize upon invasion and 2) an MLH3 structure-
583 dependent asymmetry with unequal polymerization of the two invaded strands. Several lines of
584 evidence suggest that CO designated intermediates are biased towards a CO configuration
585 independent of MutLgamma. For example, Yen1, an SSN with no inherent resolution bias in vitro,
586 generates COs with similar frequencies as MutLgamma when activated after CO designation in
587 budding yeast (Arter et al., 2018). It should also be noted that some organisms such as *Caenorhabditis*
588 *elegans* lack MutLgamma entirely and rely on SSNs for generation of interference-dependent COs
589 (Saito et al., 2013). However, we do not find an increase in SSN-dependent crossing over until after
590 dHJ formation suggesting that the MLH3 structure-dependent asymmetry is the key driver of CO biased
591 resolution in mouse spermatocytes.
592
593 In conclusion, the combination of fine-scale recombination and global cytological analysis in CO
594 maturation deficient mouse spermatocytes allowed us to discover both conserved and unique features
595 of meiotic recombination mechanisms to propel our understanding of CO intermediate processing in
596 general.
597
598 **Limitations of the study**
599 Recombination analysis in this study is limited to a single locus, the *59.5* hotspot, which is useful for
600 study due to its high frequency of meiotic DSBs on one parental homolog, density of polymorphisms,
601 and strong preference for crossing over. However, it should be noted that behavior of *59.5* may not
602 reflect genome-wide patterns of recombination. We attempted to compare all available locus-specific
603 analysis to global frequencies using cytology, but some features, such as NCOs are indistinguishable

604 cytologically. Additionally, our model of CO precursor differentiation is inferred based upon the end
605 products of recombination in mutants. As such, confirmation will depend upon further studies in wild
606 type and the development of new technologies to detect CO precursors in mammals.

607 **Figure Legends**
608

609 **Figure 1. *Exo1*$^{-/-}$ spermatocytes have reduced recombination intermediates and fewer bivalents**
610 **most of which require MLH3**

611 **(A)** Current model of mammalian DSB repair in meiosis. The double Holliday junction (dHJ) is
612 inferred based upon work in budding yeast. SDSA, synthesis-dependent strand annealing; SSN,
613 structure-selective endonuclease.

614 **(B)** Representative immunofluorescence images of zygotene stage spermatocytes of the indicated
615 genotypes stained for SYCP3 (magenta) and DMC1 (white). Scatter plot of DMC1 foci per cell
616 (y-axis) with error bars of the mean ± SD in WT (N=3, 224 ± 72.2), *Exo1*^{het} (N=2, 196.5 ± 60.45),
617 and *Exo1*$^{-/-}$ (N=4, 155.8 ± 60). P-values were determined by Kruskal-Wallis test with Dunn's
618 multiple comparison correction. *Exo1*$^{-/-}$ spermatocytes showed fewer DMC1 foci per cell on
619 average in zygonema as compared to WT and *Exo1*^{het} spermatocytes.

620 **(C)** Representative immunofluorescence images of pachytene stage spermatocytes of the indicated
621 genotypes stained for SYCP3 (magenta) and MLH1 (white). Scatter plot of MLH1 and MLH3 foci
622 per cell as above in WT (MLH1, N=3, 22.3 ± 2.5), *Exo1*^{het} (MLH1, N=3, 22.4 ± 2.3), *Exo1*$^{-/-}$
623 (MLH1, N=3, 20.0 ± 3.6) and *Exo1*^{het} (MLH3, N=2, 22.9 ± 4.1), *Exo1*$^{-/-}$ (Mlh3, N=3, 20.3 ± 3.6).
624 P-values were determined by Kruskal-Wallis test with Dunn's multiple comparison correction
625 (MLH1) and Mann-Whitney, two-tailed (MLH3). *Exo1*$^{-/-}$ spermatocytes showed fewer MLH1 and
626 MLH3 foci per cell on average in pachynema as compared to WT and *Exo1*^{het} spermatocytes.

627 **(D)** Representative metaphase images of spermatocytes from the indicated genotypes stained with
628 Giemsa. Left, scatter plot of bivalent counts per cell (y-axis) with error bars of the mean ± SD in
629 *Exo1*^{het} (N=3, 19.9 ± 0.3), *Mlh3*$^{-/-}$ (N=5, 1.4 ± 1.2), *Exo1*$^{-/-}$*Mlh3*$^{-/-}$ (N=4, 1.2 ± 1.1), and *Exo1*$^{-/-}$
630 (N=4, 5.3 ± 2.0). P-values were determined by Kruskal-Wallis test with Dunn's multiple
631 comparison correction. Right, histogram of the distribution of bivalents per cell of the indicated
632 genotypes. The x-axis shows the number of bivalents per cell and the y-axis shows the average
633 percentage of total nuclei with the indicated number of bivalents. The two graphs also visually

634 depict the Coefficient of Variation of bivalents per genotype *Mlh3*$^{-/-}$ (84%), *Exo1*$^{-/-}$*Mlh3*$^{-/-}$ (96%),
635 *Exo1*$^{-/-}$ (39.1%), and *Exo1*^{het} (1.3%). *Exo1*$^{-/-}$ spermatocytes had fewer bivalents than *Exo1*^{het} but
636 more than *Mlh3*$^{-/-}$ spermatocytes. *Exo1*$^{-/-}$*Mlh3*$^{-/-}$ analysis shows the majority of the residual
637 bivalents in *Exo1*$^{-/-}$ require MLH3.
638
639 **Figure 2. Meiotic COs are independent of EXO1 nuclease activity and residual COs in *Exo1*$^{-/-}$**
640 **spermatocytes have altered characteristics**
641 **(A)** Poisson-corrected frequencies of COs at the *59.5* hotspot are plotted per 10,000 haploid
642 genome equivalents (y-axis) with error bars of the mean ± SD in WT (N=4, 160.8 ± 37.1),
643 *Exo1*^{het} (N=4, 116.0 ± 30.2), *Exo1*$^{nd/nd}$ (N=4, 117.6 ± 23.9), *Exo1*$^{-/-}$ (N=6, 25.59 ± 7.32), *Mlh3*$^{-/-}$
644 *Exo1*$^{-/-}$ (N=4, 0.77 ± 1.56), and *Mlh3*$^{-/-}$ (N=3, 0.28 ± 0.50). P-values were determined by Fisher's
645 exact test, two-tailed. *Exo1*$^{nd/nd}$ showed similar CO frequency as *Exo1*^{het} spermatocytes, and
646 both are fertile suggesting most COs are independent of EXO1 nuclease-activity. *Exo1*$^{-/-}$ had
647 more residual COs compared to *Mlh3*$^{-/-}$ spermatocytes, and they require MLH3.
648 **(B)** COs with one haplotype switch between parental genotypes were designated as simple COs.
649 COs with one contiguous tract that scores positive for both parental genotypes were designated
650 mixed COs. Mixed COs often arise when more than one simple CO is present in a sample.
651 Mixed COs were found at the frequency expected for multiple COs per sample and were
652 therefore included with simple COs for this analysis. COs with more than two haplotype
653 switches that may involve tracts that are positive for both parental genotypes were designated
654 as complex COs. Complex COs are likely derived from a single recombination event that
655 experiences template switching or branch migration during CO formation and may include
656 retained heteroduplex. Histogram of the percent of simple (yellow) and complex (gray) CO
657 recombination patterns (y-axis) of the indicated genotypes. Frequency of complex COs in WT
658 sperm (N=6, 2.5 ± 3.5), WT Late 4C spermatocytes (N=4, 0.4 ± 0.9), *Exo1*$^{nd/nd}$ (N=4, 14.4 ± 9.7),
659 and *Exo1*$^{-/-}$ (N=6, 32.4 ± 24.1). P-values were determined by Fisher's exact test, two-tailed.

660 *Exo1*$^{-/-}$ spermatocytes had significantly more complex COs than WT and twice as many as
661 *Exo1*$^{nd/nd}$.
662 **(C)** CO breakpoint frequency in centiMorgans per Megabase (cM/Mb) is plotted on the y-axis and
663 CO breakpoint distribution plotted on the x-axis with the hotspot center set at 0 kb. The area
664 under the curve represents total CO frequency. Note the CO breakpoint map for B to D COs
665 (red, top) and D to B COs (blue, bottom) cluster on opposite sides of the hotspot center
666 indicating reciprocal CO asymmetry due to most DSBs forming on the B chromosome. Vertical
667 dotted lines mark the average location of CO breakpoints by cumulative distribution with the
668 difference between them estimating the mean CO-dependent gene conversion tract length.
669 *Exo1*$^{-/-}$ spermatocytes have a high frequency of CO breakpoints near the hotspot center and
670 concomitantly shorter estimated gene conversion tract length compared to *Exo1*^{het} or *Exo1*$^{nd/nd}$
671 spermatocytes. Top ticks, genotyped polymorphisms. n_{Tot}, total number of COs mapped.
672
673 **Figure 3. Spermatocytes lacking EXO1 or MLH3 nuclease activity have similar frequency and**
674 **distribution of bivalents**
675 Representative metaphase images of spermatocytes from the indicated genotypes stained with
676 Giemsa. Left, scatter plot of bivalent counts per cell (y-axis) with error bars of the mean ± SD in
677 *Mus81*$^{-/-}$ (N=5, 19.8 ± 0.6), *Mlh3*$^{-/-}$ (N=5, 1.4 ± 1.2), *Mlh3*$^{-/DN}$ (N=3, 3.97 ± 1.9), *Mlh3*$^{DN/DN}$ (N=3,
678 5.5 ± 1.9), *Exo1*$^{-/-}$ (N=4, 5.3 ± 2.0), and *Mus81*$^{-/-}$*Exo1*$^{-/-}$ (N=3, 4.1 ± 1.9). P-values were
679 determined by Kruskal-Wallis test with Dunn's multiple comparison correction. Right, histogram
680 of the distribution of bivalents per cell of the indicated genotypes. The x-axis shows the number
681 of bivalents per cell and the y-axis shows the average percentage of total nuclei with the
682 indicated number of bivalents. The two graphs also visually depict the CoV of bivalents per
683 genotype: *Mus81*$^{-/-}$*Exo1*$^{-/-}$ (47.8%), *Mlh3*$^{-/DN}$ (46.6%), *Exo1*$^{-/-}$ (39.1%), and *Mlh3*$^{DN/DN}$ (34.7%).
684 *Mlh3*$^{DN/DN}$ showed similar frequency and distribution of bivalents as *Exo1*$^{-/-}$ spermatocytes,
685 suggesting COs in *Exo1*$^{-/-}$ may be independent of MLH3 nuclease activity. Consistently, the

686 number of bivalents was dosage-sensitive to the copy number of *Mlh3*^{DN} supporting a structural
687 role for MLH3. Further, loss of the SSN MUS81 in addition to EXO1 (*Mus81*$^{-/-}$*Exo1*$^{-/-}$) led to
688 fewer bivalents than *Exo1*$^{-/-}$ spermatocytes, suggesting some residual COs in *Exo1*$^{-/-}$ are formed
689 by SSNs.

690 **Figure 4. Most COs in *Exo1*$^{-/-}$ spermatocytes form contemporaneously with SSN-dependent**
691 **resolvase activity**

692 **(A)** Top, isolated live testicular cells from an adult BxD mouse were stained with Hoechst 33342
693 sorted for red and blue emission by UV stimulated fluorescence activated cell sorting. The top
694 oval shows the Late 4C population and sorting gate used to enrich for diplonema and
695 metaphase. The bottom oval shows the population of 1C spermatids. Sorted samples were
696 typically ≥70% enriched for diplonema (**Table S1**). Purity of the sorted population was assessed
697 by immunofluorescence staining of spermatocyte spreads with antibodies against SYCP3 and
698 SYCP1 or gammaH2AX.
699 Bottom, sorted cells as above from an adult BxD mouse that was synchronized for meiotic entry.
700 The example here depicts sorting for a synchronized diplotene population. Quality of
701 synchronization was assessed by pre-sort spermatocyte spreads stained with SYCP3, SYCP1,
702 gammaH2AX, and Histone H1t (**Table S1**). ≥90% of enrichment for specific prophase stages
703 can be achieved by coupling synchronization with sorting. Enrichment of sorted cells was
704 similarly tested by immunofluorescence staining. A representative image of a sorted diplotene
705 stage spermatocyte is shown stained for SYCP3 and Histone H1t (H1t, inset).

706 **(B)** Histogram of the proportion of COs (normalized to the diplonema frequency) found in Late 4C
707 and enriched populations of the indicated stages of meiotic prophase from WT, *Mlh3*$^{-/-}$, and
708 *Exo1*$^{-/-}$. P-values were determined by Fisher's exact test, two-tailed. In WT, most COs appeared
709 during pachynema with no further increase in diplonema consistent with the model that
710 MutLgamma produces COs in pachynema. By contrast, in *Mlh3*$^{-/-}$, COs in pachynema account
711 for only 14.3 ± 39.2% of COs found in diplonema, consistent with the model that SSN activity is

712 retricted to either diplonema or the pachynema to diplonema transition, likely acting in a back-up
713 repair capacity. The temporal dynamics of *Exo1*$^{-/-}$ COs is like that of *Mlh3*$^{-/-}$ with COs in
714 pachynema accounting for only 39.9 ± 24.4 % of COs in diplonema. Together, the data suggest
715 that most COs in *Exo1*$^{-/-}$ spermatocytes are produced at a stage consistent with SSN activity.
716 **(C)** Histogram of co-conversion frequency found in populations enriched for the indicated stages of
717 meiosis in WT, *Mlh3*$^{-/-}$, *Hei10*$^{-/-}$, and *Exo1*$^{-/-}$. When CO formation is defective, long co-
718 conversions are formed in lieu of COs. Co-conversions are particularly apparent at hotspots like
719 *59.5* that are highly enriched for crossing over. In WT, co-conversions are found at a low
720 frequency in both pachynema and diplonema (3.8 ± 3.3 and 4.2 ± 4, respectively). By contrast,
721 in *Mlh3*$^{-/-}$, co-conversions are similarly low in pachynema but highly enriched in diplonema (5.7 ±
722 4.3 and 56.5 ± 13.7, respectively). Co-conversions are also highly prevalent in *Hei10*$^{-/-}$
723 diplonema (85.3 ± 15.0), consistent with the model that long co-conversions are derived from
724 RNF212-designated CO precursors. Like *Mlh3*$^{-/-}$, in *Exo1*$^{-/-}$ spermatocytes, co-conversions are
725 low in pachynema and highly enriched in diplonema (9.1 ± 5.1 and 40.4 ± 11.4, respectively).
726 Together, most co-conversions found in *Exo1*$^{-/-}$ and *Mlh3*$^{-/-}$ spermatocytes are likely products of
727 backup repair pathways, acting on unrepaired CO intermediates in either the pachynema to
728 diplonema transition or in diplonema. P-values were determined by Fisher's exact test, two-
729 tailed.
730 Zygonema (Z), Pachynema (P), Diplonema (D), Late 4C (4C).
731
732 **Figure 5. Co-conversion characteristics reveal features of CO precursor processing in mouse**
733 **spermatocytes**
734 **(A)** Representative population of co-conversions isolated from *Mlh3*$^{-/-}$ and *Exo1*$^{-/-}$ diplotene
735 spermatocytes. Top, Spo11 oligonucleotides mapping in reads per million in B (Lange et al.,
736 2016) shows the majority of DSBs are formed in the central 200bp of *59.5*. The blue line plots
737 the minimal and the gray line the maximal possible gene conversion tract. The x-axis shows

738 ticks marking polymorphisms at the top and relative position within the hotspot at the bottom.
739 The center of the hotspot is marked by a vertical dotted line and plotted at 0kb. Total frequency
740 ± SD (top left) and number isolated (n_{Tot}, bottom right) of co-conversions are shown. The
741 number of co-conversions plotted is proportional to their frequency for visual comparison
742 between genotypes. Asterisks mark discontinuous events. P-value was determined by Fisher's
743 exact test, two-tailed. While the frequency of co-conversion is similar between *Mlh3*$^{-/-}$ and *Exo1*$^{-/-}$
744 , the characteristics are markedly different with *Exo1*$^{-/-}$ spermatocytes having longer,
745 discontinuous tracts that frequently span the hotspot center (see below).
746 **(B)** Scatter plot of the length of co-conversions in kb (mean ± SD) in pachynema and diplonema in
747 WT (145 ± 89, 226 ± 164bp, respectively), *Mlh3*$^{-/-}$ (190 ± 157, 427 ± 239bp), *Hei10*$^{-/-}$ (ND, 292 ±
748 200bp), and *Exo1*$^{-/-}$ (223 ± 105bp, 813 ± 511bp). P-values are derived from Kruskal-Wallis test
749 with Dunn's multiple comparison correction. In *Mlh3*$^{-/-}$ and *Exo1*$^{-/-}$ spermatocytes, co-
750 conversions were longer in diplonema than pachynema, consistent with the derivation of long
751 co-conversions from back-up repair pathways acting later. Further, the diplotene stage co-
752 conversions from *Exo1*$^{-/-}$ were longer than those from *Mlh3*$^{-}$, suggesting that the upstream CO
753 precursor from which co-conversions are derived is longer in *Exo1*$^{-/-}$ than *Mlh3*$^{-/-}$ spermatocytes.
754 **(C)** Scatter plot of the length of co-conversions in kb (mean ± SD) in Late 4C from *Hfm1*$^{-/-}$ (347 ±
755 167bp), *Hei10*$^{-/-}$ (329 ± 231bp), *Mlh3*$^{-/-}$ (298 ± 230bp), *Mlh3*$^{-/-}$*Exo1*$^{-/-}$ (334 ± 288bp), *Exo1*$^{-/-}$ (692 ±
756 567bp), *Mus81*$^{-/-}$*Exo1*$^{-/-}$ (711 ± 459bp), *Mlh3*$^{-/DN}$ (613 ± 432bp), *Mlh3*$^{DN/DN}$ (619 ± 422bp), and
757 *Msh2*$^{-/-}$*Exo1*$^{-/-}$ (1111 ± 898bp). P-values are derived from Kruskal-Wallis test with Dunn's
758 multiple comparison correction. The longer co-conversions in *Exo1*$^{-/-}$ spermatocytes require
759 MLH3. *Hfm1*$^{-/-}$, *Hei10*$^{-/-}$, and *Mlh3*$^{-/-}$ have co-conversions with similar lengths, suggesting
760 mutants that lack MutLgamma focus formation do not extend the CO precursor intermediate.
761 Co-conversions from *Msh2*$^{-/-}$*Exo1*$^{-/-}$ and *Mus81*$^{-/-}$*Exo1*$^{-/-}$ have similar length to those from *Exo1*$^{-/-}$,
762 suggesting neither defective mismatch repair nor SSN-dependent resolution contributes to
763 longer co-conversions. In support of the model that MutLgamma focus formation correlates with

764 longer co-conversions and by extension longer CO precursors, co-conversions from both *Mlh3*
765 $^{-/DN}$ and *Mlh3*$^{DN/DN}$ were similarly long as those isolated from *Exo1*$^{-/-}$ spermatocytes.

766 **(D)** Histogram of the percent of continuous (salmon) and discontinuous (gray) co-conversions (CC)
767 of the indicated genotypes. Discontinuity percentage: *Hfm1*$^{-/-}$ (0 ± 0%), *Hei10*$^{-/-}$ (0 ± 0%), *Mlh3*$^{-/-}$
768 (0.8 ± 3.9%), *Mlh3*$^{-/-}$*Exo1*$^{-/-}$ (5.3 ± 6.8%), *Exo1*$^{-/-}$ (19.4 ± 23.9%), *Mus81*$^{-/-}$*Exo1*$^{-/-}$ (18.1 ± 8.5%),
769 *Mlh3*$^{-/DN}$ (14.6 ± 6.6%), *Mlh3*$^{DN/DN}$ (9.5 ± 11.8%), and *Msh2*$^{-/-}$*Exo1*$^{-/-}$ (21.5 ± 11.7%). Co-
770 conversions from diplonema and Late 4C spermatocytes were compiled and p-values were
771 determined by Fisher's exact test, two-tailed. Co-conversions were considered discontinuous
772 when there were two or more contiguous tracts in the same sample, as these were present at a
773 higher frequency than expected by chance. Co-conversions from *Hfm1*$^{-/-}$ and *Hei10*$^{-/-}$ had
774 similarly low frequency of discontinuity as *Mlh3*$^{-/-}$ spermatocytes, whereas *Exo1*$^{-/-}$, *Mus81*$^{-/-}$*Exo1*$^{-}$
775 $^{/-}$, *Mlh3*$^{-/DN}$, and *Msh2*$^{-/-}$*Exo1*$^{-/-}$ were more frequently discontinuous. Co-conversions from *Mlh3*$^{-/-}$
776 *Exo1*$^{-/-}$ spermatocytes were more discontinuous than *Mlh3*$^{-/-}$ but less than *Exo1*$^{-/-}$. Discontinuity
777 of co-conversions is the only phenotype where *Mlh3* is not epistatic to *Exo1* suggesting
778 discontinuity is primarily driven by template switching during elongation of the CO precursor and
779 is partially caused by defective MMR.

780 **(E)** Histogram of the distribution of the minimum gene conversion tracts of co-conversions (CC) with
781 respect to the hotspot center. P-values were determined by Fisher's exact test, two-tailed. Top,
782 all co-conversions. Bottom, to correct for differences in polymorphism density between the left
783 and right side of the hotspot center, polymorphism locations were mirror-inverted with respect to
784 co-conversions, and only those that would have remained detectable were included. No bias in
785 3' end invasion of DSBs were observed after correcting for polymorphism density. *Exo1*$^{-/-}$*-like*
786 mutants had more co-conversions that span the hotspot center than those from *Mlh3*$^{-/-}$*-like*
787 mutants. We suggest that in *Mlh3*$^{-/-}$*-like* mutants polymerization occurs from only one of the 3'
788 ends, whereas in *Exo1*$^{-/-}$*-like* mutants extension occurs from both 3' ends.

789 **(F)** Representative co-conversions and their corresponding dispensation after mirror-inverting
790 polymorphism positions. Bottom, relative position within the *59.5* hotspot. Black ticks (top) mark
791 the original polymorphism locations and magenta vertical doted lines and ticks (bottom) mark
792 the mirror-inverted polymorphism locations. The hotspot center is indicated with a black vertical
793 line and mapped at '0". Co-conversions were categorized into 4 groups: Type-1) one-sided co-
794 conversions that would not have been detected, Type-2) one-sided co-conversions that would
795 remain detected, Type-3) co-conversions that span the hotspot center originally, but would be
796 detected as one-sided with inverted polymorphisms, and Type-4) co-conversions that span the
797 hotspot center originally and would remain detected as spanning after inverting polymorphisms.
798 **(G)** Scatter plot showing the fraction of each gene conversion tract contributing to either the long or
799 short arm of the co-conversions (CC) that span the hotspot center. This marked skew in the
800 distribution of co-conversions is likely caused by differential polymerization from the
801 independent 3' ends.
802
803 **Figure 6. Model illustrating CO precursor differentiation and maturation in mouse**
804 **spermatocytes**
805 Either 3' end of the DSB is equally likely to invade the homolog to form the CO-designated
806 intermediate - the single-end invasion (SEI). In pachynema, the invaded 3' end extends via
807 polymerization for ~300bp forming an extended SEI (eSEI) intermediate. Formation of the eSEI
808 is MLH3 independent, but invasion/extension of the second 3' end to generate a nicked double
809 Holliday junction (dHJ) depends upon MLH3's structural function. This second round of
810 polymerization extends both invaded 3' ends but asymmetrically, to a total length of ~600bp.
811 This nicked dHJ is more capable of being resolved as a CO via SSN-mediated resolution.
812 Finally, we suggest that during resolution, nicking by MLH3 directs strand processing and
813 mismatch repair that reorients CO breakpoints symmetrically on either side of the hotspot center
814 with few or no haplotype switches. By contrast, SSN-dependent resolution lacks the ability to

815 reorient CO breakpoints as observed in *Exo1*$^{-/-}$- and *Mlh3*$^{-/-}$-like spermatocytes. The vertical
816 black dotted line represents the location of the originating DSB.
817
818 **Figure S1. Axis lengths, recombination frequencies, and interference measurements**
819 **(A)** Scatter plot of the axis lengths per cell measured in microns (mean ± SD) in WT (185.8 ± 23.6)
820 and *Exo1*$^{-/-}$ (186.0 ± 24.8). *Exo1*$^{-/-}$ spermatocytes had similar axis lengths as WT.
821 **(B)** Histogram plot of total recombination frequency (per 10,000 haploid genome equivalents) for the
822 indicated genotype categorized into COs (pink), co-conversions (green) and singletons (blue).
823 Total recombination frequencies were similar among WT sperm (244.6), WT diplonema (213.4),
824 and mutants including *Rnf212*$^{-/-}$ Late 4C (196), *Hei10*$^{-/-}$ diplonema (211.6), *Mlh3*$^{-/-}$ diplonema
825 (194.6), and *Exo1*$^{-/-}$ diplonema (193.7). P-values were determined by Fisher's exact test, two-
826 tailed.
827 **(C)** Plot of mean coefficient of coincidence (CoC) versus inter-interval distance calculated by
828 measuring MLH1 focus distribution of the indicated genotypes. We saw that MLH1 foci from
829 *Exo1*$^{-/-}$ (top right, and bottom – scale adjusted) spermatocytes show similar interference as WT.
830 SP (sperm), D (diplonema), 4C (Late 4C).
831
832 **Figure S2. Inferred CO breakpoints from co-conversions in *Exo1*$^{-/-}$ spermatocytes have similar**
833 **distribution as *Exo1*$^{-/-}$ COs**
834 Top, cumulative distribution curves of CO breakpoints in the B to D (red) and D to B (blue)
835 orientations from *Exo1*^{het}, *Exo1*$^{-/-}$, and inferred hypothetical breakpoints from co-conversions in
836 *Exo1*$^{-/-}$spermatocytes. The mean of each CO breakpoint distribution is indicated with a dotted
837 line. The hotspot center is indicated with black dashed line and plotted at 0kb. Bottom, CO
838 breakpoint maps for *Exo1*^{het}, *Exo1*$^{-/-}$, and inferred hypothetical breakpoints using co-conversions
839 from *Exo1*$^{-/-}$ spermatocytes. The inferred gene conversion tract length based upon hypothetical
840 CO breakpoints from *Exo1*$^{-/-}$ co-conversions (127bp) was much shorter than the directly

841 measured co-conversion tract length of 692 ± 567bp. This shorter estimate was like the
842 apparent estimated CO gene conversion tract length of *Exo1*$^{-/-}$ COs (182bp). This suggests that
843 reciprocal CO asymmetry does not estimate gene conversion tract length for COs in *Exo1*$^{-/-}$
844 spermatocytes owing to the higher breakpoint frequency near the hotspot center. Taken
845 together, reciprocal CO asymmetry only accurately estimates gene conversion tract length when
846 CO breakpoint distributions are evenly distributed away from the hotspot center, such as is
847 found when MutLgamma is proficient. CentiMorgans/Megabase (cM/Mb).
848

849 **Figure S3. Representative co-conversions isolated from all mutants**

850 Representative co-conversion plots isolated from the indicated genotypes and meiotic prophase
851 stage. All mapped recombinants are included in the Supplementary Data File. The blue line
852 plots the minimal and the gray line the maximal possible gene conversion tract. The x-axis
853 shows ticks marking polymorphisms at the top and relative position within the hotspot at the
854 bottom. The center of the hotspot (PRDM9 binding site polymorphism) is marked by a vertical
855 dotted line and plotted at 0kb. Total frequency ± SD (top left) and number isolated (n_{Tot}, top
856 right) of co-conversions are shown. The number of co-conversions plotted is proportional to their
857 frequency for visual comparison between genotypes. Diplotene samples were used wherever
858 possible given their higher purity than Late 4C in general. Co-conversions are short and rare in
859 WT or mutants that lack CO designation (RNF212), and common in CO maturation deficient
860 mutants.

861 **Methods**

862 **Mice**

863 Experimental animals, C57BL/6J x DBA/2J (BxD) F1 hybrid male mice were generated by crossing
864 inbred mouse strains C57BL/6J (B) and DBA/2J (D). Single mutants (*Exo1*$^{-/-}$, *Hfm1*$^{-/-}$, *Hei10*$^{-/-}$, *Rnf212*$^{-/-}$,
865 *Mlh3*$^{-/-}$, *Mlh3*$^{DN/DN}$) were generated from independently maintained heterozygous mice in the B and D
866 strains that were genotyped to verify homozygosity of the corresponding haplotype for the *59.5* hotspot.
867 Double mutants, (*Mlh3*$^{-/-}$ *Exo1*$^{-/-}$, *Mus81*$^{-/-}$ *Exo1*$^{-/-}$, *Msh2*$^{-/-}$ *Exo1*$^{-/-}$) were generated similarly from mice
868 independently maintained as heterozygous for both genes in both strains. *Mlh3*$^{-/DN}$ were generated by
869 crossing *Mlh3*$^{+/-}$ with *Mlh3*$^{+/DN}$ mice from the D and B strains, respectively. *Msh2*$^{-/-}$ were generated by
870 crossing *Msh2.1*$^{tm2.1Rak/J}$ with *Stra8-cre* and were maintained as a null line in both strains.

871

872 **Spermatocyte spreads and immunofluorescence**

873 This protocol was performed as described (Zelazowski et al., 2017). Briefly, whole or part of
874 decapsulated testes were digested with collagenase (2mg/ml) in 2ml of testis isolation medium (TIM)
875 for 55' at 32°C while shaken at 500rpm. (TIM: 104mM NaCl, 45mM KCl, 1.2mM MgSO4, 0.6mM
876 KH2PO4, 0.1% (w/v) glucose, 6mM sodium lactate, 1mM sodium pyruvate, pH 7.3, filter sterilized).
877 These extracted tubules were washed three times with 15ml TIM, then digested with Trypsin (0.7
878 mg/ml) in 2ml TIM containing DNAse I (4 μg/ml) for 15' at 32°C/500rpm. This digestion was stopped by
879 adding Trypsin inhibitor to a final concentration of 4 mg/ml in TIM and an additional 50μl of 0.4 μg/μl
880 DNAse I was added to the mix. The suspension was then aspirated for 2' with a transfer pipette and
881 then filtered through 70-micron cell strainer to separate the cells. The cells were pelleted and washed
882 twice in TIM containing DNAse I (1 μg/ml), and then resuspended in PBS. The amount of PBS used
883 was proportional to the starting tissue, and typically 12-15ml was used for a whole WT testis and 3-6ml
884 for mutant testis. The cells were then resuspended and incubated in hypotonic, 0.1M sucrose
885 prewarmed to 37°C for 3-5'. In the meantime, a moist flat chamber was prepared and 65μl of 1% PFA
886 (pH 9.2)/0.1% Triton X-100 laid onto glass slides. The sucrose cell suspension was then transferred to

887 these glass slides, ~20ul per slide. These slides remain in the closed moist chamber for 2.5 hours, then
888 with the lid ajar for 30', then with the lid open for an additional 30'. Slides were then washed with water
889 containing 1:250 Photo-Flo 200 and air-dried before storage at -80°C.

890 For antibody staining, the slides were blocked with antibody dilution buffer (ADB) for 30' at 37°C
891 in a moist flat chamber. (ADB: 10% goat serum, 3% BSA, 0.05% Triton X-100, 1xPBS). Slides were
892 then incubated with primary antibody diluted in ADB either overnight at room temperature or for 1 hr at
893 37°C. The slides were washed once with 1xPBS/0.4% Photo-Flo 200, then once with 1xPBS/0.4%
894 Photo-Flo 200/0.01% Triton X-100, for 5' each. Slides were blocked with ADB for 10' at 37°C and then
895 incubated with secondary antibody diluted in ADB. Upon secondary antibody treatment, slides were
896 maintained in the dark. Slides were washed with 1xPBS/0.4% Photo-Flo 200 and then with
897 1xPBS/0.4% Photo-Flo 200/ 0.01% Triton X-100, for 5' as described above. These slides were then air-
898 dried and mounted with coverslips using Prolong Gold antifade containing DAPI.

899

900 **Metaphase spreads**

901 This protocol was performed as previously described (Zelazowski et al., 2017). Briefly, whole or part of
902 decapsulated testes were incubated at room temperature in a 2.9% isotonic sodium citrate solution.
903 The tubules were pulled apart until sufficient cells were released into the solution, making it turbid. The
904 supernatant was then transferred to a 15ml tube while avoiding tubules and pelleted. Cells were
905 resuspended in 1% hypotonic sodium citrate solution for 12' at room temperature. Cells were pelleted,
906 resuspended, thoroughly mixed, and incubated in fixative for 5' (Fixative: 3 parts 200 proof ethanol, 1
907 parts glacial acetic acid, 0.025 parts chloroform). After the first incubation, cells were resuspended and
908 incubated in fresh fixative for 5'. Approximately 20μl of this suspension was dropped on a grease-free
909 slide, air-dried, and stained with mild shaking in 1:20 dilution Giemsa in 1x PBS (pH 6.5) for 45'. Slides
910 were then briefly washed with water, dried, and mounted with a cover slip for imaging.

911

912 **Synchronization of spermatogenesis**

913 Mouse spermatocytes were synchronized as described (Hogarth et al., 2013; Patel et al., 2019). Briefly,
914 WIN 18,446 was pipet fed to 1-3 days postpartum (dpp) BxD F1 male neonates at 100μg/g body weight
915 for seven (or more, if needed for weight gain) consecutive days every 22 - 24 hours. Starting on the 8th
916 day of treatment, if the mice weighed at least 4g, they were intraperitoneally injected with 200μg of
917 retinoic acid suspended in 10μl dimethyl sulfoxide. The duration of days post-injection that allows
918 enrichment for specific prophase stages was determined based on published reports on spermatocyte
919 prophase timing (Hogarth, 2013) and experimentation. Typically, synchrony is maintained for at least 6
920 rounds of spermatogenesis allowing isolation of adult populations. For synchronization of *Hei10*$^{-/-}$,
921 *Rnf212*$^{-/-}$, *Mlh3*$^{-/-}$ and *Exo1*$^{-/-}$, male neonates from experimental crosses were genotyped between 0-
922 2dpp to test for the presence of animals homozygous for null allele before treatment.
923
924 **Isolation of stage-specific and Late 4C spermatocytes by flow cytometry**
925 Spermatocytes were isolated as described in earlier reports (Cole et al., 2014; Zelazowski et al., 2017).
926 Briefly, seminiferous tubules from decapsulated testis were digested with 0.5 mg/ml collagenase in
927 Gey's Balanced Salt Solution (GBSS) for 15 minutes at 33°C, while shaking at 500 RPM. For
928 collagenase digestion and most subsequent steps, ~10ml of GBSS was used per decapsulated WT or
929 mutant mouse testis. These tubules were then washed once with GBSS, followed by digestion with
930 trypsin at 0.5 mg/ml in GBSS supplemented with 1 μl/ml DNase I, for 15 minutes at 33°C/500 RPM.
931 Subsequently, Newborn Calf Serum (NCS) is added to a concentration of 5% to inactivate Trypsin. To
932 individualize cells, the solution was pipetted up and down for 3' with a transfer pipette and then filtered
933 through a 70-micron cell strainer. Cells were then washed multiple times in GBSS with 5% NCS/1 μg/ml
934 DNAse I and subsequently stained by incubating in a solution of 5 μg/ml Hoechst 33342 in GBSS with
935 5% NCS/1 μg/ml DNAse I for 45' minutes at 33°C/500 RPM. The amount of Hoechst staining solution
936 was proportional to tissue weight, 6ml and 3ml were typically used for staining one WT or mutant testis,
937 respectively. After Hoechst staining, propidium iodide was added to a final concentration of 0.2 μg/ml
938 and the cells were filtered through a 70-micron cell strainer. Cells were then sorted in a BD Aria or BD

939 Fusion flow cytometer, with UV 350nm argon laser. On a linear scale, blue (DNA content) and red
940 (chromosome compaction) emission spectra were used to gate for different stages of meiosis, with for
941 example, leptonema appearing closest to the left and diplonema the right of the red emission spectrum.
942 Isolation of synchronized mouse spermatocytes produces the highest purity of specific stages; however
943 the gating strategy can successfully enrich for late stages (pachynema and diplonema) albeit with a
944 slight loss in purity by comparison. Empirical optimization by combining the sort-gating strategy and
945 subsequent purity analysis is required to optimize and verify sample enrichment. Sorted cells were
946 washed with PBS, pelleted at 600g for 5', and snap-frozen as a dry pellet in dry ice/ethanol slurry for
947 storage at -80°C. A portion, typically 5,000-20,000 cells were surface spread and stained with
948 antibodies (SYCP3/SYCP1/Histone H1t/gammaH2AX) and DAPI to test for the purity of the sorted
949 population.
950
951 **Genomic DNA isolation**
952 The genomic DNA was isolated as previously described (Zelazowski et al., 2017). Cell pellets were
953 resuspended in 500μl 0.2x SSC, pH 7 (SSC 20x: 3M NaCl and 0.3M citric acid trisodium salt
954 dihydrate). For this suspension, 60μL β-mercaptoethanol, 10μL of 20 mg/ml Proteinase K and 50μL of
955 10% SDS were added sequentially and incubated for 30' at 55°C/500rpm. This cell digest was then
956 extracted with Phenol/chloroform/isoamyl alcohol. DNA was then precipitated with two volumes of ice-
957 cold 100% ethanol with linear polyacrylamide as a DNA carrier. The DNA pellet was washed with 70%
958 ethanol, air-dried for ~5', and resuspended overnight in 5mM Tris (pH 7.5) at 4°C.
959
960 **Determining amplification efficiency of DNA**
961 Amplification efficiency on isolated DNA was performed as described (Cole and Jasin, 2011). Briefly,
962 using nanodrop estimate of DNA concentration as a starting point and 12pg DNA (2 diploid genome
963 equivalents) as input per PCR reaction, 24-48 PCR reactions were performed. The amplification
964 consisted of 2 rounds of nested PCRs, with conditions identical to those used for NCO/CO

965 amplification. Each round of this PCR consisted of one allele-specific primer (ASP) and one universal
966 primer, and hence amplification efficiency estimated this way applies only to these primary and
967 secondary ASPs. The amplified products were run on a gel and the number of negative wells were
968 counted. The amplification adjustment factor is then given by ($-\log_2$(Number of negative wells/Number
969 of total wells))/2. For maximum reproducibility, amplification adjustment factor must fall between 0.2
970 and 0.8, if not amplifiable DNA concentration is revised and the amplification efficiency test is repeated.
971

972 **CO assay**

973 CO assay was performed as described (Cole and Jasin, 2011; Cole et al., 2010). Sperm and
974 spermatocyte DNA was analyzed in sufficiently small pools such that the number of wells with more
975 than one crossover was kept to a minimum. As such, input DNA was higher in CO defective mutants
976 like *Exo1*$^{-/-}$ (~100 genomic DNA equivalents) and *Mlh3*$^{-/-}$ (~300) as compared to *Exo1*$^{nd/nd}$ (~40). The
977 primer annealing temperature was empirically determined for each batch of 11.1x buffer. For each
978 primary PCR reaction (8μl) DNA was added to 1x buffer (10x: 450mM Tris-HCl pH 8.8, 110mM
979 (NH4)2SO4, 45mM MgCl2, 67mM Beta-mercaptoethanol, 44μM EDTA, 10mM each: dATP, dTTP,
980 dGTP, and dCTP, and 1.13 mg/ml non-acetylated BSA), 12.5mM Tris-base, 0.2μM of each primer,
981 0.25U of Taq, and 0.05U of Pfu polymerase. 2μl of the primary PCR reaction was digested with S1
982 nuclease (10μl reaction): 0.7U/μl S1 nuclease in 1x buffer: 20mM sodium acetate, 1mM Zn acetate,
983 0.1M NaCl, and the reaction was diluted and stopped with 45μL of dilution buffer (10mM Tris-HCl pH
984 7.5 and 5 μg/ml sonicated salmon sperm DNA). 1.6μl of the diluted primary PCR was used as input for
985 secondary PCR using identical conditions as described above but with nested ASPs. The secondary
986 PCR plate wells were tested for amplification, by running a 1/10 of the reaction on a 1% agarose gel.
987 Tertiary PCR (30μl) was performed on positive secondary PCR wells. The PCR program for primary,
988 secondary, and tertiary PCRs were denaturation (96°C, 1' for the first denaturation and 20'' for
989 subsequent steps), annealing (30'' at optimized temperature), extension (65°C, 1' per kb). Both primary
990 and secondary PCRs had 27 cycles of amplification, while the tertiary PCR had 30 cycles of

991 amplification. The tertiary PCR plate, in its 96 well format is then dot blotted to positively charged nylon
992 membrane to genotype by southern blotting using allele-specific oligos (ASO) probes. An equal amount
993 of somatic DNA was used as the negative control.
994
995 **NCO assay**
996 NCO assay was done as described (Cole and Jasin, 2011; Cole et al., 2010). NCOs were amplified
997 much like the COs described above, except for a few key differences: 1) The primer pairs used have
998 one ASP and one universal primer for unbiased amplification of COs, NCOs, and non-recombinant
999 DNA; 2) The input DNA was no higher than 30 haploid genome equivalents per well, so the
1000 recombinant signal was detectable over the non-recombinant background; 3) NCO assays include only
1001 a primary (8μl) and secondary (30μl) PCRs without intervening S1 nuclease digestion, with 27 and 36
1002 cycles of amplification, respectively; and 4) The entire secondary PCR was dot blotted and genotyped
1003 by Southern blotting using ASO probes.
1004
1005 **Genotyping with ASO probes**
1006 Genotyping amplicons from CO/NCO assays were done as described (Cole and Jasin, 2011; Cole et
1007 al., 2010). The ASOs were radiolabeled with T4 polynucleotide kinase in a 10μl reaction (Buffer: 70mM
1008 Tris-HCl, pH 7.5, 10mM MgCl2, 5mM spermidine trichloride, 2mM dithiothreitol; 8ng ASO; 0.35μL T4
1009 polynucleotide kinase (10U/μl), 0.2μL γ-32P-ATP (10mCi/ml)) per two blots. Reaction was done at 37°C
1010 for 45-60' and was stopped with 20μl stop buffer (25mM EDTA, 0.1% SDS, 10μM ATP) and then 20μL
1011 of unlabeled ASO of the opposite genotype (8 μg/ml) was added to the mix.
1012 Dot blot membranes were rinsed in 2X SSC (20x: 3M NaCl and 0.3M citric acid trisodium salt
1013 dihydrate) and pre-hybridized for 15' with Tetramethylammonium Chloride (TMAC) hybridization buffer
1014 (3M TMAC, 0.6% SDS, 10mM NaPO4 pH 6.8, 1mM EDTA, 4 μg/ml yeast RNA, in 5x Denhardt's
1015 solution) at 56°C for 10–15'. 50x Denhardt's solution: 1% (w/v) Ficoll 400, 1% (w/v) polyvinyl
1016 pyrrolidone, 1% (w/v) BSA (Fraction V); filter sterilized. Next, the buffer was replaced with fresh TMAC

1017 hybridization buffer with sonicated salmon sperm DNA at a concentration of 8.4 μg/ml, and incubated
1018 for 10' at 53°C. Radio-labeled ASOs were then added, and incubated for 45-60' at 53°C. Next, the blots
1019 were washed thrice with TMAC wash buffer (3M TMAC, 0.6% SDS, 10mM NaPO4 pH 6.8, 1mM
1020 EDTA), within a span of ~20' while incubating the blots at 56°C. For the final wash, the blots were
1021 incubated with TMAC wash buffer for 15' at 56°C. Blots were rinsed twice with 2X SSC, excess liquid
1022 was blotted away, wrapped in plastic and exposed overnight on a phosphorimager screen.
1023

1024 **Cytological analysis**

1025 Immunofluorescence experiments were performed blinded. All animals were BxD. Mutants and controls
1026 within an experimental set were analyzed by one individual to reduce inter-experimentalist variation.
1027 Only on axis (SYCP3-associated) foci were counted and any X/Y MLH1 or MLH3 foci were excluded
1028 from the analysis.

1029 For DMC1 foci, SYCP3 staining was used to stage cells and zygonema cells were chosen such
1030 that some chromosomes have contiguous SYCP3 axis and were categorized as early-mid zygonema
1031 (<50% synapsis, visually estimated) or mid-late zygonema (>50% synapsis, visually estimated). Similar
1032 numbers (Fishers Exact test, two-tailed, ns) of each zygotene stage were compared between WT (38
1033 and 39, respectively), *Exo1*^{het} (16 and 24 respectively), and *Exo1*$^{-/-}$ (33 and 40, respectively).

1034 For MLH1 and MLH3 foci, every cell that was positive for foci were counted.

1035 Metaphase bivalents counts were performed blinded as much as possible by comparing
1036 together mutants with similar severity of CO loss (for example, *Mlh3*$^{DN/DN}$ and *Exo1*$^{-/-}$*Mus81*$^{-/-}$). To
1037 minimize inter-experimentalist variation, the authors agreed upon a common strategy for counting. To
1038 ensure we only analyzed intact nuclei, independent chromosomes structures were quantified first as
1039 'objects' and subsequently were categorized as either bivalents or univalents. A cell was then included
1040 only if the number of total bivalents and univalents accounted for all chromatids expected (40 for mouse
1041 spermatocytes). Cells that had chromosome structures that the author was unable to classify as a
1042 bivalent or univalent were not included in the analysis.

1043 Co-efficient of Coincidence (CoC) analysis was done as described (White et al., 2017). Briefly,
1044 the DAPI rich end of each chromosome (centromere) was designated the starting point and the
1045 distance of each focus from the start and length of the chromosome axis was quantified manually using
1046 ImageJ. Based on the number of MLH1 foci per micron axis and cells counted (61 and 42 cells for WT
1047 and *Exo1*$^{-/-}$, respectively), 10 intervals per bivalent were assessed. The Mean CoC vs inter-interval
1048 distance was calculated using MATLAB (White et al., 2017). Axis lengths for WT and *Exo1*$^{-/-}$
1049 spermatocytes (**Figure S1A**) were acquired from the CoC dataset.
1050

1051 **Experimental design, quantification, and statistical analysis**

1052 Cytological analyses were performed blinded, and samples were cross checked by independent
1053 experimentalists. For recombination analysis, NCO and CO plates from samples of different mutants
1054 were amplified, hybridized, and genotyped by Southern blotting together to reduce inter-experimental
1055 variation. While the genotyping of recombinants wasn't blinded, most mutants had similar severity of
1056 CO loss and different phenotypes weren't apparent until results were fully tabulated.
1057 All data are shown as means with standard deviation and 95% confidence intervals. The p-value
1058 is shown when the difference was significant and are adjusted for multiple comparisons as appropriate.
1059 Broadly, we used Fisher's exact test, two-tailed for categorical comparisons. To compare means, we
1060 used Mann-Whitney for pairwise and Kruskal-Wallis followed by Dunn's multiple comparison correction
1061 for non-pairwise comparisons. We have reported the tests performed in text and figure legends. We
1062 show the number of animals analyzed as capital 'N', and number of quantified data points as small 'n'.
1063 For most conditions, at least three animals were analyzed per genotype and all animals were BxD.

1064 **Acknowledgments**

1065 We thank P. Cohen for mice and the MLH3 antibody, W. Edelmann, N. Hunter, and R. Pezza for mice,
1066 M.A. Handel for the H1t antibody, and members of the Cole lab for comments on the manuscript. We
1067 also thank N. Kleckner, N. Hunter, G.V. Börner, J. Ahuja, and A. Villeneuve for sharing their insights.
1068 This work was supported by National Institutes of Health grants R01HD098129 and DP2HD087943

(F.C.) and summer undergraduate fellowship R25CA181004 (H.D.), the Cockrell Endowment (T.P.) and H.E.B Fellowships (T.P. and M.F.), CPRIT grant R1213 (F.C.) and training grant RP170067 (R.K., V.K., I.Y.). We acknowledge the National Institutes of Health CA16672 for support of the Research Animal Support Facility Smithville and the CPRIT RP170628 for support of the Flow Cytometry and Cellular Imaging Core.

Author contributions

T.P., L.P., R.K., E.H., H.D., I.F., I.O., H.N., M.F., and P.C. conducted experiments; T.P., and F.C. performed statistical analyses; and T.P., L.P., R.K., and F.C. designed the experiments and analyzed the data. T.P. and F.C. wrote the paper.

Declaration of interests

The authors declare that they have no competing interest

References

Ahuja, J.S., Harvey, C.S., Wheeler, D.L., and Lichten, M. (2021). Repeated strand invasion and extensive branch migration are hallmarks of meiotic recombination. Mol Cell *81*, 4258-4270 e4254.

Allers, T., and Lichten, M. (2001). Differential timing and control of noncrossover and crossover recombination during meiosis. Cell *106*, 47-57.

Amin, N.S., Nguyen, M.N., Oh, S., and Kolodner, R.D. (2001). exo1-Dependent mutator mutations: model system for studying functional interactions in mismatch repair. Mol Cell Biol *21*, 5142-5155.

Argueso, J.L., Wanat, J., Gemici, Z., and Alani, E. (2004). Competing crossover pathways act during meiosis in Saccharomyces cerevisiae. Genetics *168*, 1805-1816.

Arter, M., Hurtado-Nieves, V., Oke, A., Zhuge, T., Wettstein, R., Fung, J.C., Blanco, M.G., and Matos, J. (2018). Regulated Crossing-Over Requires Inactivation of Yen1/GEN1 Resolvase during Meiotic Prophase I. Developmental cell *45*, 785-800 e786.

Baudat, F., and de Massy, B. (2007). Cis- and trans-acting elements regulate the mouse Psmb9 meiotic recombination hotspot. PLoS Genet *3*, e100.

Bell, L.R., and Byers, B. (1983). Homologous association of chromosomal DNA during yeast meiosis. Cold Spring Harb Symp Quant Biol *47 Pt 2*, 829-840.

Borner, G.V., Kleckner, N., and Hunter, N. (2004). Crossover/noncrossover differentiation, synaptonemal complex formation, and regulatory surveillance at the leptotene/zygotene transition of meiosis. Cell *117*, 29-45.

Cannavo, E., Sanchez, A., Anand, R., Ranjha, L., Hugener, J., Adam, C., Acharya, A., Weyland, N., Aran-Guiu, X., Charbonnier, J.B.*, et al.* (2020). Regulation of the MLH1-MLH3 endonuclease in meiosis. Nature *586*, 618-622.

Cole, F., Baudat, F., Grey, C., Keeney, S., de Massy, B., and Jasin, M. (2014). Mouse tetrad analysis provides insights into recombination mechanisms and hotspot evolutionary dynamics. Nature genetics *46*, 1072-1080.

Cole, F., and Jasin, M. (2011). Isolation of meiotic recombinants from mouse sperm. Methods Mol Biol *745*, 251-282.

Cole, F., Kauppi, L., Lange, J., Roig, I., Wang, R., Keeney, S., and Jasin, M. (2012a). Homeostatic control of recombination is implemented progressively in mouse meiosis. Nat Cell Biol *14*, 424-430.

Cole, F., Keeney, S., and Jasin, M. (2010). Comprehensive, fine-scale dissection of homologous recombination outcomes at a hot spot in mouse meiosis. Mol Cell *39*, 700-710.

Cole, F., Keeney, S., and Jasin, M. (2012b). Preaching about the converted: how meiotic gene conversion influences genomic diversity. Ann N Y Acad Sci *1267*, 95-102.

Crown, K.N., McMahan, S., and Sekelsky, J. (2014). Eliminating both canonical and short-patch mismatch repair in Drosophila melanogaster suggests a new meiotic recombination model. PLoS Genet *10*, e1004583.

De Muyt, A., Jessop, L., Kolar, E., Sourirajan, A., Chen, J., Dayani, Y., and Lichten, M. (2012). BLM helicase ortholog Sgs1 is a central regulator of meiotic recombination intermediate metabolism. Mol Cell *46*, 43-53.

Furman, C.M., Elbashir, R., and Alani, E. (2021). Expanded roles for the MutL family of DNA mismatch repair proteins. Yeast *38*, 39-53.

Garcia, V., Phelps, S.E., Gray, S., and Neale, M.J. (2011). Bidirectional resection of DNA double-strand breaks by Mre11 and Exo1. Nature *479*, 241-244.

Gioia, M., Payero, L., Pannafino, G., Chen, J.J., Salim, S., Fajith, G., Farnaz, A.F., Momoh, S., Scotland, M., Raghavan, V.*, et al.* (2021). Exo1-protected DNA nicks direct crossover formation in meiosis. bioRxiv, 2021.2008.2029.458102.

Goellner, E.M., Putnam, C.D., and Kolodner, R.D. (2015). Exonuclease 1-dependent and independent mismatch repair. DNA Repair (Amst) *32*, 24-32.

Gray, S., and Cohen, P.E. (2016). Control of Meiotic Crossovers: From Double-Strand Break Formation to Designation. Annu Rev Genet *50*, 175-210.

Guillon, H., Baudat, F., Grey, C., Liskay, R.M., and de Massy, B. (2005). Crossover and noncrossover pathways in mouse meiosis. Mol Cell *20*, 563-573.

Guillon, H., and de Massy, B. (2002). An initiation site for meiotic crossing-over and gene conversion in the mouse. Nature genetics *32*, 296-299.

Guiraldelli, M.F., Eyster, C., Wilkerson, J.L., Dresser, M.E., and Pezza, R.J. (2013). Mouse HFM1/Mer3 is required for crossover formation and complete synapsis of homologous chromosomes during meiosis. PLoS Genet *9*, e1003383.

Hassold, T., and Hunt, P. (2001). To err (meiotically) is human: the genesis of human aneuploidy. Nat Rev Genet *2*, 280-291.

Hogarth, C.A. (2013). Transcriptional/translational regulation of mammalian spermatogenic stem cells. Adv Exp Med Biol *786*, 105-128.

Hogarth, C.A., Evanoff, R., Mitchell, D., Kent, T., Small, C., Amory, J.K., and Griswold, M.D. (2013). Turning a spermatogenic wave into a tsunami: synchronizing murine spermatogenesis using WIN 18,446. Biol Reprod *88*, 40.

Holloway, J.K., Booth, J., Edelmann, W., McGowan, C.H., and Cohen, P.E. (2008). MUS81 generates a subset of MLH1-MLH3-independent crossovers in mammalian meiosis. PLoS Genet *4*, e1000186.

Holloway, J.K., Sun, X., Yokoo, R., Villeneuve, A.M., and Cohen, P.E. (2014). Mammalian CNTD1 is critical for meiotic crossover maturation and deselection of excess precrossover sites. J Cell Biol *205*, 633-641.

Hunter, N. (2015). Meiotic Recombination: The Essence of Heredity. Cold Spring Harb Perspect Biol *7*.

Hunter, N., and Kleckner, N. (2001). The single-end invasion: an asymmetric intermediate at the double-strand break to double-holliday junction transition of meiotic recombination. Cell *106*, 59-70.

Jeffreys, A.J., and May, C.A. (2004). Intense and highly localized gene conversion activity in human meiotic crossover hot spots. Nature genetics *36*, 151-156.

Jeffreys, A.J., and Neumann, R. (2002). Reciprocal crossover asymmetry and meiotic drive in a human recombination hot spot. Nature genetics *31*, 267-271.

Kan, R., Sun, X., Kolas, N.K., Avdievich, E., Kneitz, B., Edelmann, W., and Cohen, P.E. (2008). Comparative analysis of meiotic progression in female mice bearing mutations in genes of the DNA mismatch repair pathway. Biol Reprod *78*, 462-471.

Keelagher, R.E., Cotton, V.E., Goldman, A.S., and Borts, R.H. (2011). Separable roles for Exonuclease I in meiotic DNA double-strand break repair. DNA Repair (Amst) *10*, 126-137.

Keeney, S., Lange, J., and Mohibullah, N. (2014). Self-organization of meiotic recombination initiation: general principles and molecular pathways. Annu Rev Genet *48*, 187-214.

Kirkpatrick, D.T., Ferguson, J.R., Petes, T.D., and Symington, L.S. (2000). Decreased meiotic intergenic recombination and increased meiosis I nondisjunction in exo1 mutants of Saccharomyces cerevisiae. Genetics *156*, 1549-1557.

Kulkarni, D.S., Owens, S.N., Honda, M., Ito, M., Yang, Y., Corrigan, M.W., Chen, L., Quan, A.L., and Hunter, N. (2020). PCNA activates the MutLgamma endonuclease to promote meiotic crossing over. Nature *586*, 623-627.

Lange, J., Yamada, S., Tischfield, S.E., Pan, J., Kim, S., Zhu, X., Socci, N.D., Jasin, M., and Keeney, S. (2016). The Landscape of Mouse Meiotic Double-Strand Break Formation, Processing, and Repair. Cell *167*, 695-708 e616.

Lipkin, S.M., Moens, P.B., Wang, V., Lenzi, M., Shanmugarajah, D., Gilgeous, A., Thomas, J., Cheng, J., Touchman, J.W., Green, E.D.*, et al.* (2002). Meiotic arrest and aneuploidy in MLH3-deficient mice. Nature genetics *31*, 385-390.

Manhart, C.M., Ni, X., White, M.A., Ortega, J., Surtees, J.A., and Alani, E. (2017). The mismatch repair and meiotic recombination endonuclease Mlh1-Mlh3 is activated by polymer formation and can cleave DNA substrates in trans. PLoS biology *15*, e2001164.

Marsolier-Kergoat, M.C., Khan, M.M., Schott, J., Zhu, X., and Llorente, B. (2018). Mechanistic View and Genetic Control of DNA Recombination during Meiosis. Mol Cell *70*, 9-20 e26.

Martini, E., Borde, V., Legendre, M., Audic, S., Regnault, B., Soubigou, G., Dujon, B., and Llorente, B. (2011). Genome-wide analysis of heteroduplex DNA in mismatch repair-deficient yeast cells reveals novel properties of meiotic recombination pathways. PLoS Genet *7*, e1002305.

Martini, E., Diaz, R.L., Hunter, N., and Keeney, S. (2006). Crossover homeostasis in yeast meiosis. Cell *126*, 285-295.

Mimitou, E.P., and Keeney, S. (2018). S1-seq Assay for Mapping Processed DNA Ends. Methods Enzymol *601*, 309-330.

Myler, L.R., Gallardo, I.F., Zhou, Y., Gong, F., Yang, S.H., Wold, M.S., Miller, K.M., Paull, T.T., and Finkelstein, I.J. (2016). Single-molecule imaging reveals the mechanism of Exo1 regulation by single-stranded DNA binding proteins. Proc Natl Acad Sci U S A *113*, E1170-1179.

Nishant, K.T., Plys, A.J., and Alani, E. (2008). A mutation in the putative MLH3 endonuclease domain confers a defect in both mismatch repair and meiosis in Saccharomyces cerevisiae. Genetics *179*, 747-755.

Paiano, J., Wu, W., Yamada, S., Sciascia, N., Callen, E., Paola Cotrim, A., Deshpande, R.A., Maman, Y., Day, A., Paull, T.T.*, et al.* (2020). ATM and PRDM9 regulate SPO11-bound recombination intermediates during meiosis. Nat Commun *11*, 857.

Patel, L., Kang, R., Rosenberg, S.C., Qiu, Y., Raviram, R., Chee, S., Hu, R., Ren, B., Cole, F., and Corbett, K.D. (2019). Dynamic reorganization of the genome shapes the recombination landscape in meiotic prophase. Nat Struct Mol Biol *26*, 164-174.

Peterson, S.E., Keeney, S., and Jasin, M. (2020). Mechanistic Insight into Crossing over during Mouse Meiosis. Mol Cell *78*, 1252-1263 e1253.

Qiao, H., Prasada Rao, H.B., Yang, Y., Fong, J.H., Cloutier, J.M., Deacon, D.C., Nagel, K.E., Swartz, R.K., Strong, E., Holloway, J.K.*, et al.* (2014). Antagonistic roles of ubiquitin ligase HEI10 and SUMO ligase RNF212 regulate meiotic recombination. Nature genetics *46*, 194-199.

Raghavan, V. (2019). Incompatibilities in Mismatch Repair Genes MLH1-PMS1 Contribute to a Wide Range of Mutation Rates in Human Isolates of Baker's Yeast (Ann Arbor: Cornell University), pp. 166.

Rao, H.B., Qiao, H., Bhatt, S.K., Bailey, L.R., Tran, H.D., Bourne, S.L., Qiu, W., Deshpande, A., Sharma, A.N., Beebout, C.J.*, et al.* (2017). A SUMO-ubiquitin relay recruits proteasomes to chromosome axes to regulate meiotic recombination. Science *355*, 403-407.

Reynolds, A., Qiao, H., Yang, Y., Chen, J.K., Jackson, N., Biswas, K., Holloway, J.K., Baudat, F., de Massy, B., Wang, J.*, et al.* (2013). RNF212 is a dosage-sensitive regulator of crossing-over during mammalian meiosis. Nature genetics *45*, 269-278.

Saito, T.T., Lui, D.Y., Kim, H.M., Meyer, K., and Colaiacovo, M.P. (2013). Interplay between structure-specific endonucleases for crossover control during Caenorhabditis elegans meiosis. PLoS Genet *9*, e1003586.

Schwacha, A., and Kleckner, N. (1995). Identification of double Holliday junctions as intermediates in meiotic recombination. Cell *83*, 783-791.

Shao, H., Baitinger, C., Soderblom, E.J., Burdett, V., and Modrich, P. (2014). Hydrolytic function of Exo1 in mammalian mismatch repair. Nucleic Acids Res *42*, 7104-7112.

Sokolsky, T., and Alani, E. (2000). EXO1 and MSH6 are high-copy suppressors of conditional mutations in the MSH2 mismatch repair gene of Saccharomyces cerevisiae. Genetics *155*, 589-599.

Stahl, F.W., Foss, H.M., Young, L.S., Borts, R.H., Abdullah, M.F., and Copenhaver, G.P. (2004). Does crossover interference count in Saccharomyces cerevisiae? Genetics *168*, 35-48.

Svetlanov, A., Baudat, F., Cohen, P.E., and de Massy, B. (2008). Distinct functions of MLH3 at recombination hot spots in the mouse. Genetics *178*, 1937-1945.

Toledo, M., Sun, X., Brieno-Enriquez, M.A., Raghavan, V., Gray, S., Pea, J., Milano, C.R., Venkatesh, A., Patel, L., Borst, P.L.*, et al.* (2019). A mutation in the endonuclease domain of mouse MLH3 reveals novel roles for MutLgamma during crossover formation in meiotic prophase I. PLoS Genet *15*, e1008177.

Tran, P.T., Erdeniz, N., Dudley, S., and Liskay, R.M. (2002). Characterization of nuclease-dependent functions of Exo1p in Saccharomyces cerevisiae. DNA Repair (Amst) *1*, 895-912.

Tran, P.T., Simon, J.A., and Liskay, R.M. (2001). Interactions of Exo1p with components of MutLalpha in Saccharomyces cerevisiae. Proc Natl Acad Sci U S A *98*, 9760-9765.

Wang, S., Lee, K., Gray, S., Zhang, Y., Tang, C., Morrish, R.B., Tosti, E., van Oers, J., Amin, M.R., Cohen, P.E.*, et al.* (2022). Role of EXO1 nuclease activity in genome maintenance, the immune response and tumor suppression in Exo1D173A mice. Nucleic Acids Res.

Wang, S., Zickler, D., Kleckner, N., and Zhang, L. (2015). Meiotic crossover patterns: obligatory crossover, interference and homeostasis in a single process. Cell Cycle *14*, 305-314.

Ward, J.O., Reinholdt, L.G., Motley, W.W., Niswander, L.M., Deacon, D.C., Griffin, L.B., Langlais, K.K., Backus, V.L., Schimenti, K.J., O'Brien, M.J.*, et al.* (2007). Mutation in mouse hei10, an e3 ubiquitin ligase, disrupts meiotic crossing over. PLoS Genet *3*, e139.

Wei, K., Clark, A.B., Wong, E., Kane, M.F., Mazur, D.J., Parris, T., Kolas, N.K., Russell, R., Hou, H., Jr., Kneitz, B.*, et al.* (2003). Inactivation of Exonuclease 1 in mice results in DNA mismatch repair defects, increased cancer susceptibility, and male and female sterility. Genes & development *17*, 603-614.

White, M.A., Wang, S., Zhang, L., and Kleckner, N. (2017). Quantitative Modeling and Automated Analysis of Meiotic Recombination. Methods Mol Biol *1471*, 305-323.

Yamada, S., Hinch, A.G., Kamido, H., Zhang, Y., Edelmann, W., and Keeney, S. (2020). Molecular structures and mechanisms of DNA break processing in mouse meiosis. Genes & development *34*, 806-818.

Zakharyevich, K., Ma, Y., Tang, S., Hwang, P.Y., Boiteux, S., and Hunter, N. (2010). Temporally and biochemically distinct activities of Exo1 during meiosis: double-strand break resection and resolution of double Holliday junctions. Mol Cell *40*, 1001-1015.

Zakharyevich, K., Tang, S., Ma, Y., and Hunter, N. (2012). Delineation of joint molecule resolution pathways in meiosis identifies a crossover-specific resolvase. Cell *149*, 334-347.

Zelazowski, M.J., Sandoval, M., Paniker, L., Hamilton, H.M., Han, J., Gribbell, M.A., Kang, R., and Cole, F. (2017). Age-Dependent Alterations in Meiotic Recombination Cause Chromosome Segregation Errors in Spermatocytes. Cell *171*, 601-614 e613.

Zhao, X., Zhang, Y., Wilkins, K., Edelmann, W., and Usdin, K. (2018). MutLgamma promotes repeat expansion in a Fragile X mouse model while EXO1 is protective. PLoS Genet *14*, e1007719.

Stage	Genotype (N)[a]	Singletons (molecules tested)	Singleton Frequency $x10^{-4}$ ± SD[b] (CI, 95%)[c]	Co-conversions (molecules tested)	Co-conversion Frequency $x10^{-4}$ ± SD (CI, 95%)	COs (molecules tested)	CO Frequency $x10^{-4}$ ± SD (CI, 95%)
[d]P	Wild type (3)	96 (18,079)	74.2 ± 14.0 (60.2 to 88.2)	4 (18,079)	3.8 ± 3.3 (0.5 to 7.1)	298 (18,079)	206.6 ± 21.6 (185 to 228.2)
[e]D	Wild type (3)	94 (15,695)	72.7 ± 21.5 (51.2 to 94.2)	5 (15,695)	4.2 ± 4 (0.2 to 8.2)	190 (15,695)	136.4 ± 43.8 (92.6 to 180.2)
[f]Late 4C	Wild type (4)	104 (16,721)	73.2 ± 15.8 (57.4 to 89)	9 (16,721)	6.8 ± 4.6 (2.2 to 11.4)	238 (16,721)	160.8 ± 37.1 (123.7 to 197.9)
[g]SP	Wild type (6)	126 (22,099)	70.8 ± 18.3 (52.5 to 89.1)	16 (22,099)	9.5 ± 6.0 (3.5 to 15.5)	311 (22,099)	164.3 ± 43.4 (120.9 to 207.7)
P	*Mlh3*$^{-/-}$ (3)	161 (17,610)	92.3 ± 17.8 (74.5 to 110.1)	10 (17,610)	5.7 ± 4.3 (1.4 to 10)	1 (240,971)	0.04 ± 0.11 (-0.07 to 0.15)
D	*Mlh3*$^{-/-}$ (3)	152 (11,162)	137.9 ± 23.2 (114.7 to 161.1)	62 (11,162)	56.5 ± 13.7 (42.8 to 70.2)	11 (353,598)	0.28 ± 0.50 (-0.22 to 0.78)
D	Hei10$^{-/-}$ (4)	224 (18,298)	124.7 ± 20.2 (104.5 to 144.9)	150 (18,298)	85.3 ± 15.0 (70.3 to 100.3)	3 (18,298)	1.6 ± 1.4 (0.2 to 3.0)
Late 4C	Hei10$^{-/-}$ (4)	172 (18,621)	93.8 ± 16.4 (77.4 to 110.2)	60 (18,621)	31.7 ± 9.2 (22.5 to 40.9)	0 (18,621)	0
P	*Exo1*$^{-/-}$ (3)	86 (9,952)	87.6 ± 18.8 (68.8 to 106.4)	9 (9,952)	9.1 ± 5.1 (4 to 14.2)	9 (9,952)	9.0 ± 5.5 (3.5 to 14.5)
D	*Exo1*$^{-/-}$ (3)	123 (9,805)	130.6 ± 22.1 (108.5 to 152.7)	38 (9,805)	40.4 ± 11.4 (31.6 to 55.4)	22 (9,805)	22.7 ± 10.8 (11.9 to 33.5)
Late 4C	*Exo1*^{het} (4)	101 (8,370)	131.9 ± 32.6 (99.3 to 164.5)	7 (8,370)	9.31 ± 9.4 (6.6 to 12.4)	91 (8,370)	116.0 ± 30.2 (85.8 to 146.2)
Late 4C	*Exo1*nd (4)	256 (9,301)	293.8 ± 54.6 (239.2 to 348.4)	12 (9,301)	13.8 ± 11.8 (2 to 25.6)	193 (18,026)	117.6 ± 23.9 (93.7 to 141.5)
Late 4C	*Exo1*$^{-/-}$ (6)	409 (14,683)	288.0 ± 45.6 (242.4 to 333.6)	65 (14,683)	49.1 ± 22.4 (30.8 to 77.2)	145 (59,769)	25.59 ± 7.32 (18.27 to 32.91)
Late 4C	*Exo1*$^{-/-}$ *Mlh3*$^{-/-}$ (4)	391 (12,909)	310.0 ± 43.1 (266.9 to 353.1)	55 (12,909)	43.6 ± 15.3 (31 to 62.4)	1 (12,909)	0.77 ± 1.56 (0 to 2.33)
Late 4C	*Exo1*$^{-/-}$ *Mus81*$^{-/-}$ (2)	64 (5,949)	111.2 ± 21.6 (89.6 to 132.8)	22 (5,949)	38.2 ± 11.9 (29.2 to 54)	12 (5,949)	20.3 ± 9.2 (11.1 to 29.5)
Late 4C	*Exo1*$^{-/-}$ *Msh2*$^{-/-}$ (3)	142 (10,331)	146.8 ± 23.1 (123.7 to 169.9)	50 (10,331)	51.7 ± 12.6 (41.8 to 67.8)	23 (10,331)	22.6 ± 9.0 (13.6 to 31.6)
Late 4C	*Mlh3*$^{-/DN}$ (3)	99 (10,259)	100.4 ± 18.3 (82.1 to 118.7)	47 (10,259)	47.7 ± 12.2 (37.2 to 62)	15 (10,259)	14.7 ± 6.9 (7.8 to 21.6)
Late 4C	*Mlh3*$^{DN/DN}$ (2)	59 (6,075)	100.7 ± 20.0 (80.7 to 120.7)	19 (6,075)	32.3 ± 10.6 (24.5 to 46.7)	12 (6,075)	19.9 ± 9.0 (10.9 to 28.9)
Late 4C	*Hfm1*$^{-/-}$ (4)	276 (13,018)	215.2 ± 41.4 (173.8 to 256.6)	28 (13,018)	21.7 ± 13.5 (8.2 to 35.2)	1 (13,018)	0.77 ± 1.5 (0 to 2.27)
Late 4C	*Mlh3*$^{-/-}$ (6)	419 (16,487)	258.3 ± 41.1 (217.2 to 299.4)	57 (16,487)	33.8 ± 13.4 (21.3 to 48.7)	0 (16,487)	0

59.5 BU. [a]N, number of animals tested. [b]SD, standard deviation. [c]CI, confidence interval. [d]P, pachynema. [e]D, diplonema. [f]Late 4C, diplonema and metaphase. [g]SP, sperm.

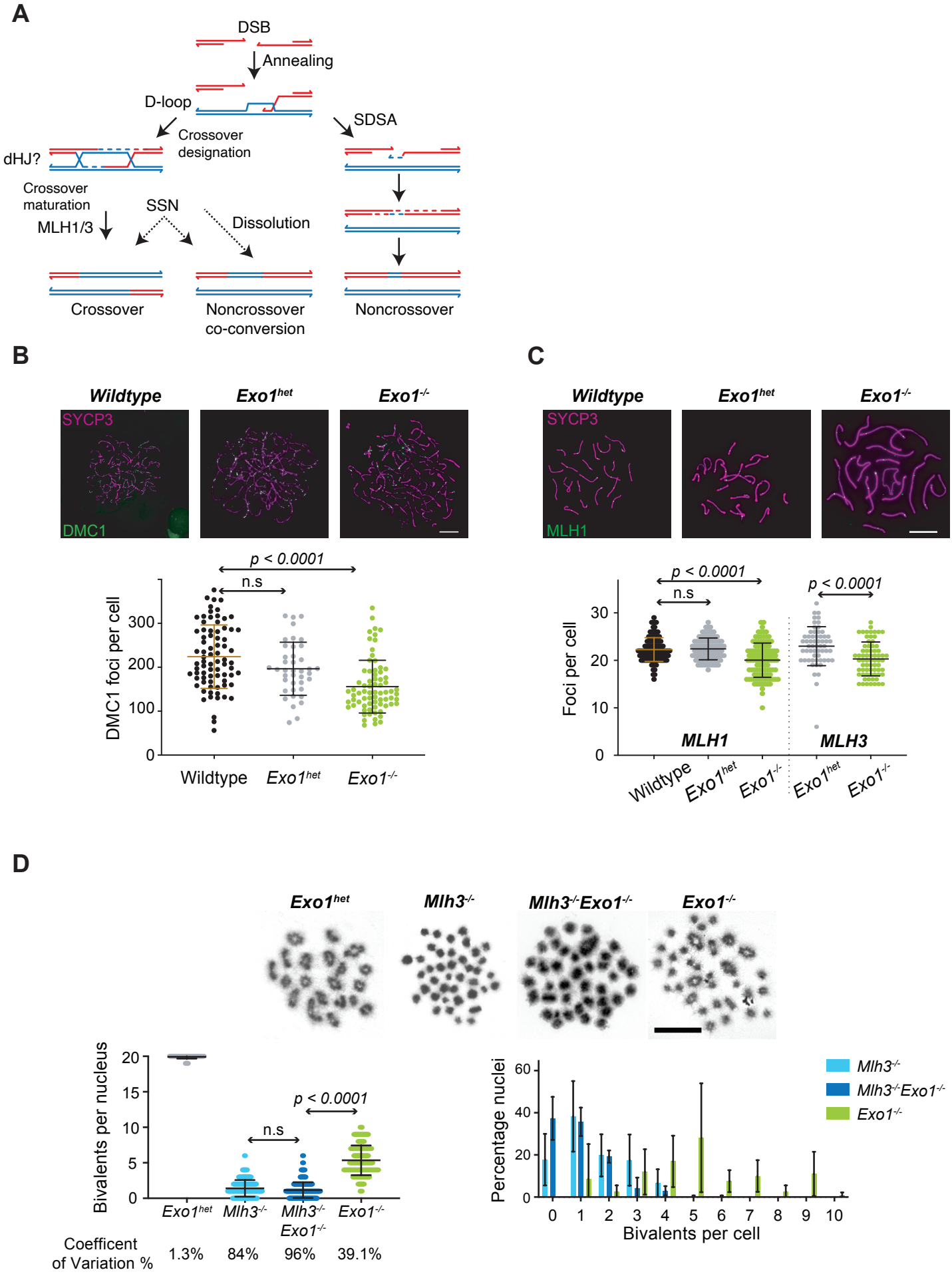

Figure 1 Exo1_Premkumar et al

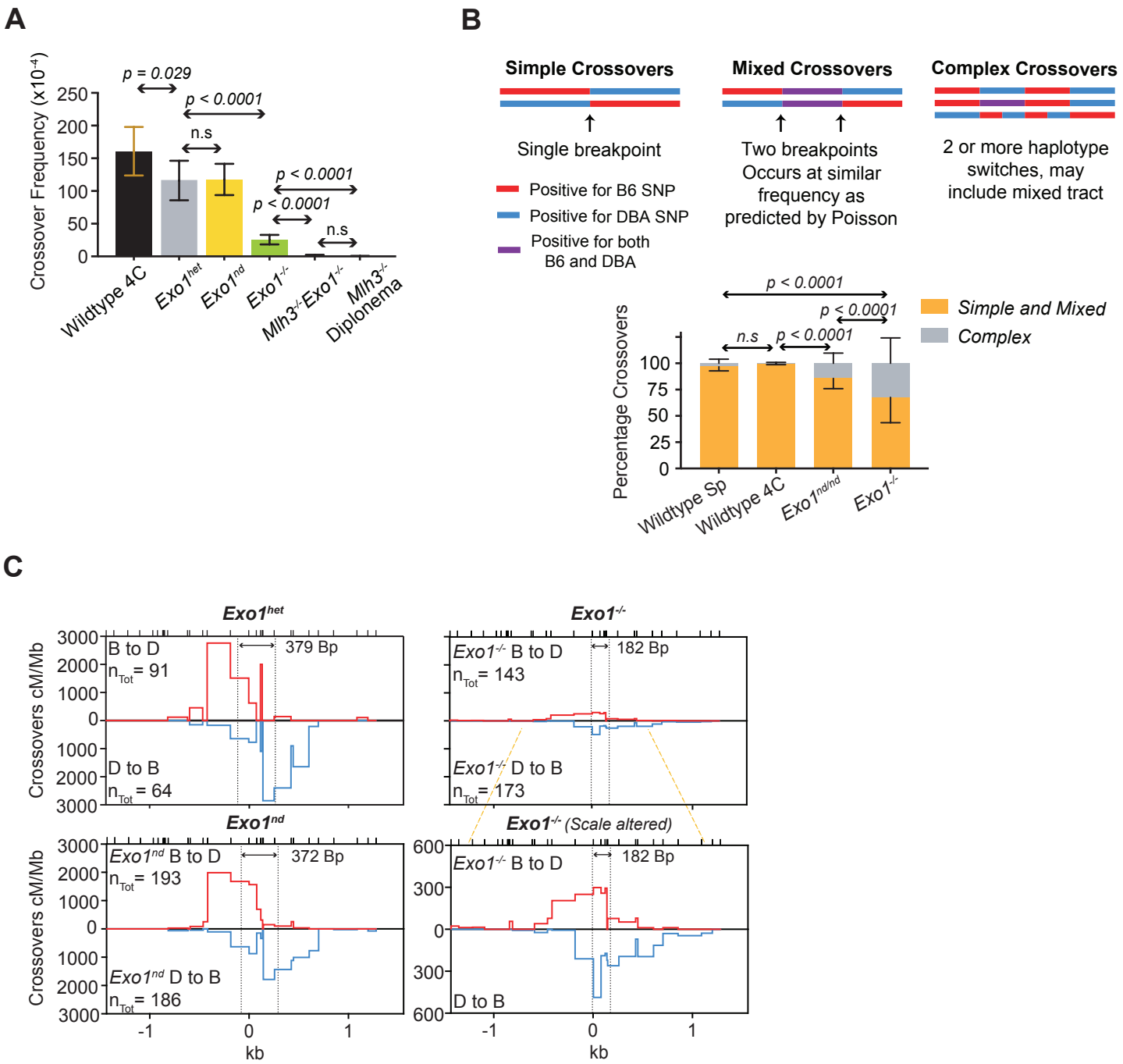

Figure 2 Premkumar et al

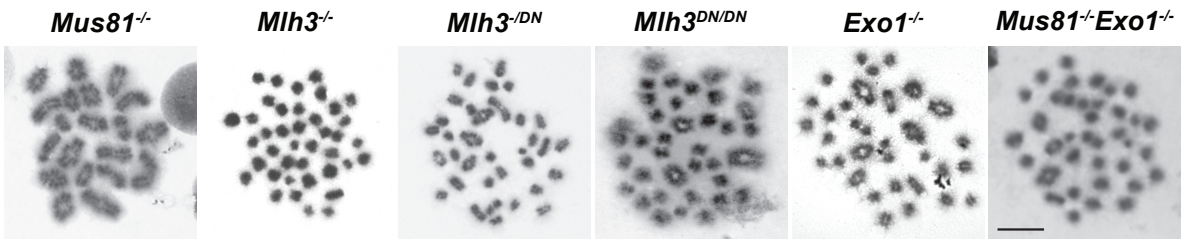

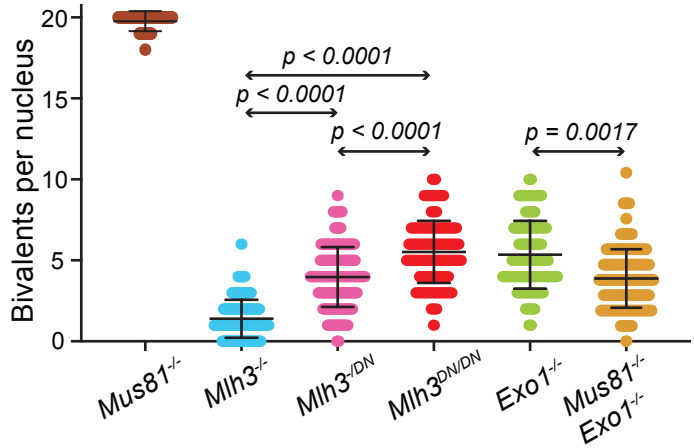

	Mus81-/-	Mlh3-/-	Mlh3-/DN	Mlh3DN/DN	Exo1-/-	Mus81-/-Exo1-/-
Coefficent of Variation %	2.1%	84%	46.6%	34.7%	39.1%	46.6%

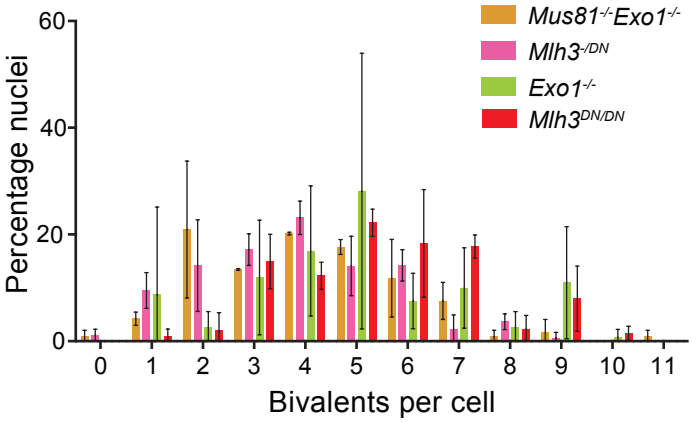

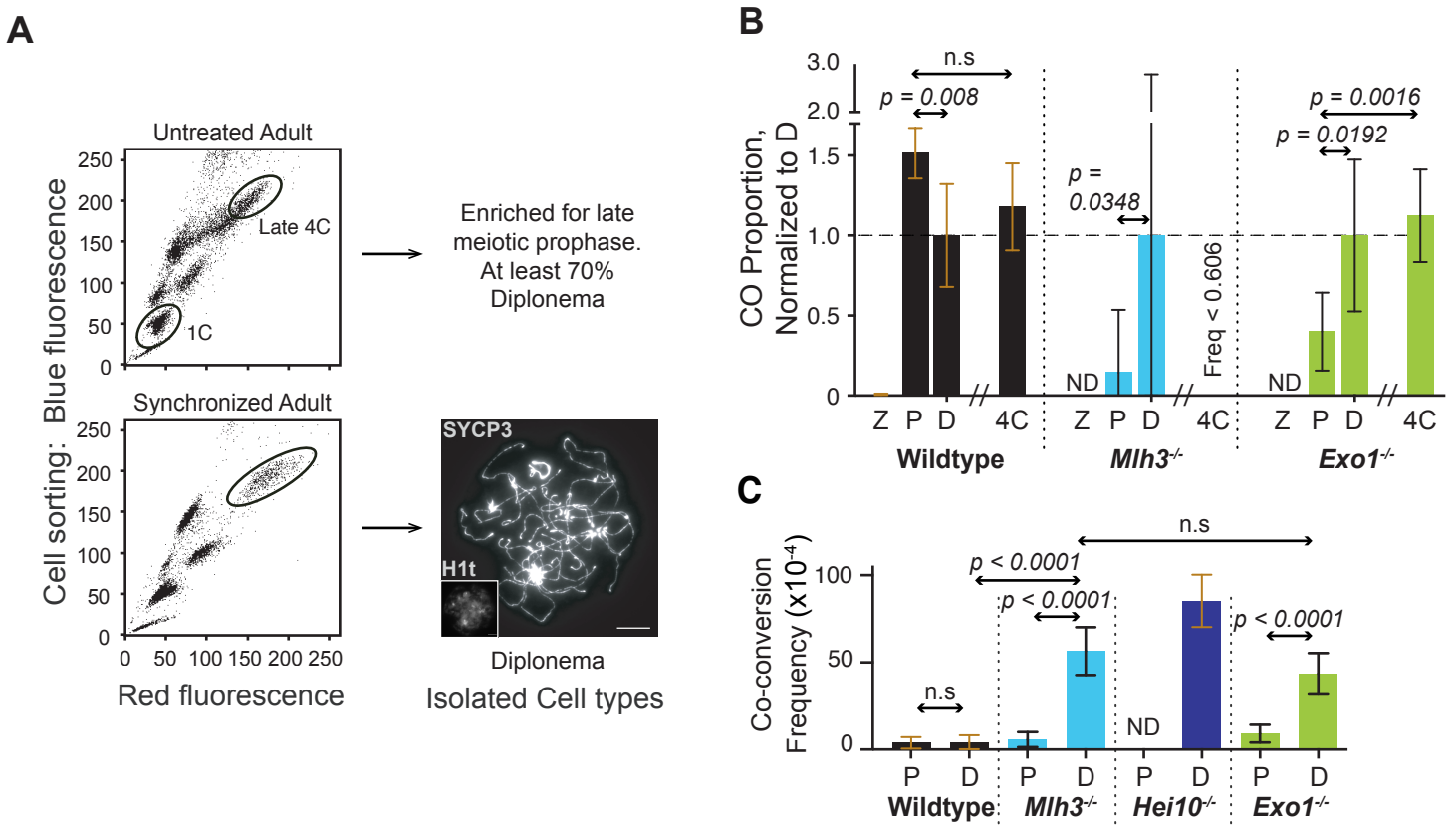
A
Untreated Adult
Late 4C
1C
Synchronized Adult
Cell sorting: Blue fluorescence
Red fluorescence
Enriched for late meiotic prophase. At least 70% Diplonema
SYCP3
H1t
Diplonema
Isolated Cell types
B
CO Proportion, Normalized to D
n.s
p = 0.008
p = 0.0348
p = 0.0016
p = 0.0192
Freq < 0.606
ND
Z P D 4C
Wildtype
Mlh3-/-
Exo1-/-
C
Co-conversion Frequency (x10-4)
p < 0.0001
n.s
P D
Wildtype
Mlh3-/-
Hei10-/-
Exo1-/-

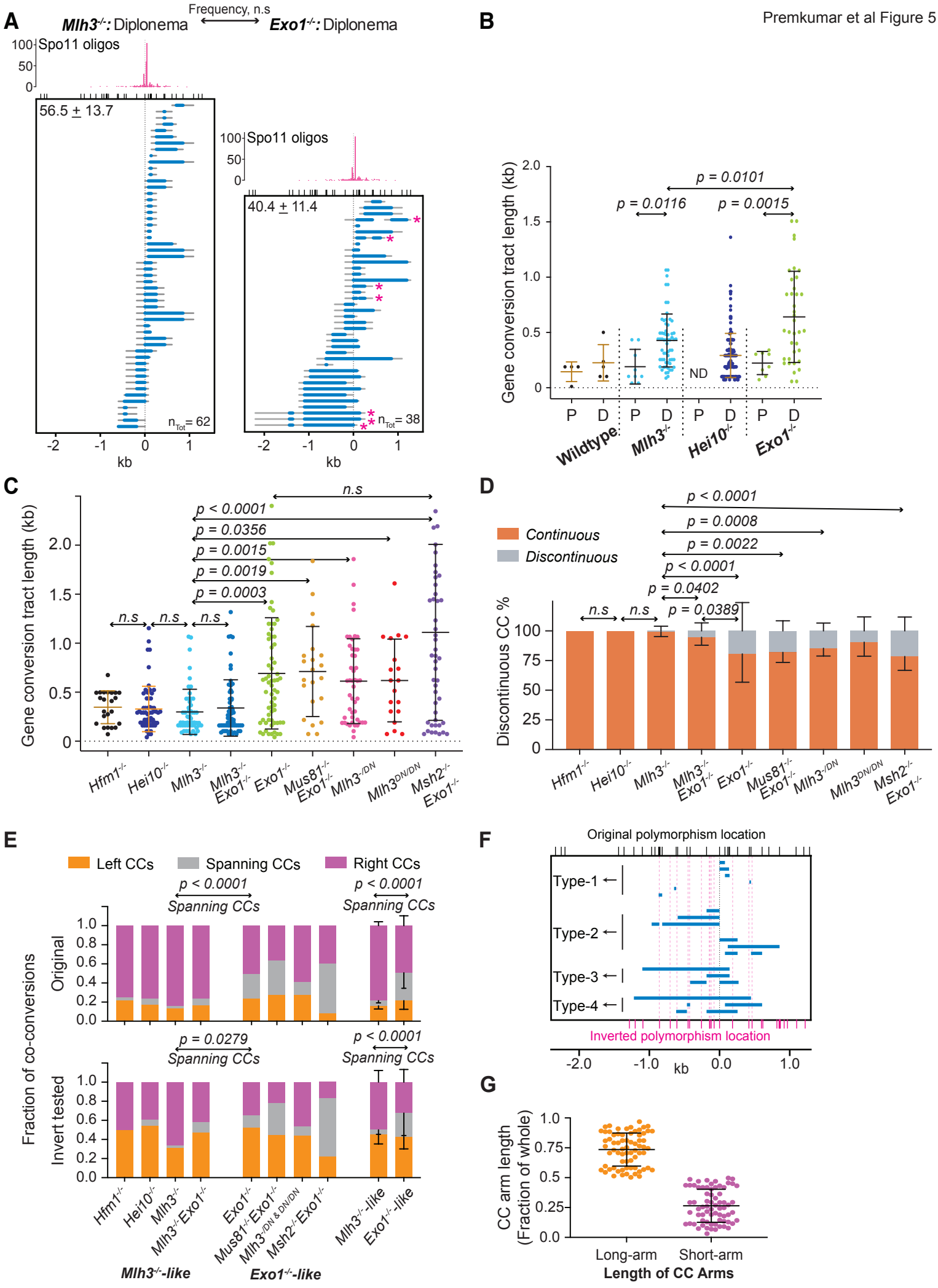
A
Frequency, n.s
Mlh3-/-: Diplonema
Exo1-/-: Diplonema
Spo11 oligos
56.5 ± 13.7
40.4 ± 11.4
n_Tot = 62
n_Tot = 38
kb
B
Gene conversion tract length (kb)
p = 0.0101
p = 0.0116
p = 0.0015
ND
P
D
Wildtype
Mlh3-/-
Hei10-/-
Exo1-/-
C
Gene conversion tract length (kb)
n.s
p < 0.0001
p = 0.0356
p = 0.0015
p = 0.0019
p = 0.0003
Hfm1-/-
Hei10-/-
Mlh3-/-
Mlh3-/- Exo1-/-
Exo1-/-
Mus81-/- Exo1-/-
Mlh3-/DN
Mlh3DN/DN
Msh2-/- Exo1-/-
D
Continuous
Discontinuous
Discontinuous CC %
p < 0.0001
p = 0.0008
p = 0.0022
p < 0.0001
p = 0.0402
p = 0.0389
E
Left CCs
Spanning CCs
Right CCs
Original
Invert tested
Fraction of co-conversions
p < 0.0001
p = 0.0279
Mlh3-/--like
Exo1-/--like
F
Original polymorphism location
Type-1
Type-2
Type-3
Type-4
Inverted polymorphism location
kb
G
CC arm length (Fraction of whole)
Long-arm
Short-arm
Length of CC Arms

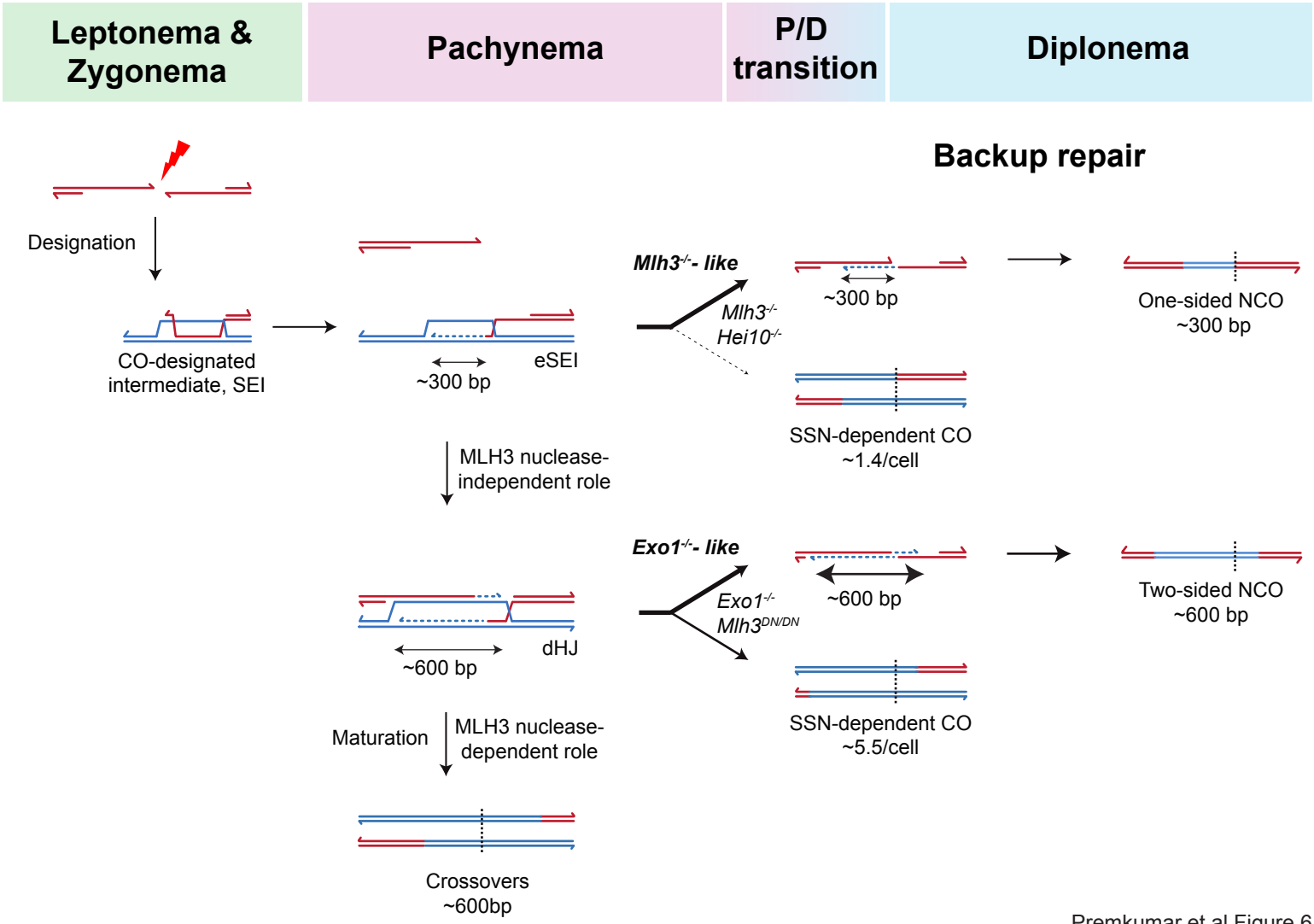

Premkumar et al Figure 6